Materials Advances

ROYAL SOCIETY OF CHEMISTRY

PAPER

View Article Online
View Journal | View Issue

Cite this: *Mater. Adv.*, 2026, 7, 1066

Re-entrant structural phase transition and charge carrier conduction in $La_{2-x}Sr_xFeMnO_6$ solid solutions for electronic device applications

Baniya R. Meena and Anup K. Ghosh *

This research explores the structural, dielectric, and electrical transport characteristics of polycrystalline $La_{2-x}Sr_xFeMnO_6$ compounds with varying strontium concentrations (x = 0.0, 0.1, 0.2, 0.5, 1.0, 1.5, and 2.0). These compounds were prepared through the solid-state reaction technique at high temperatures. Rietveld refinement of their XRD data confirms a re-entrant structural phase transition (cubic–rhombohedral–cubic) induced by Sr doping. The vibrational study of $(Fe/Mn)O_6$ octahedra was carried out by Raman and FTIR spectroscopies. X-ray photoelectron spectroscopy (XPS) results demonstrated the presence of mixed valence oxidation states (+3 and +4) of Fe and Mn cations in the measured samples. The temperature-dependent resistivity data of these compounds have been explained by the long-range electron hopping and short-range polaron hopping conduction mechanisms at high- and low-temperature regions, respectively. Their dielectric constant (ε') exhibits dispersion behavior, which is attributed to the Maxwell–Wagner interfacial polarization and hopping mechanism of charge carriers. The leakage current density has been explained on the basis of Ohmic conduction mechanism and space-charge-limited conduction (SCLC) mechanism. All these studied properties are strongly influenced by structural distortion-induced strain, oxygen vacancies, Schottky defects, and possible charge ordering. The low leakage current density of these materials with a high dielectric constant make them promising for application in electronic devices.

Received 8th August 2025,
Accepted 26th November 2025

DOI: 10.1039/d5ma00868a

rsc.li/materials-advances

1. Introduction

Nowadays, advanced materials are becoming increasingly important in a broad range of electronic and energy storage applications. In the near future, the development of energy storage and memory devices is expected to rely on giant dielectric materials possessing high dielectric permittivity (ε'). Perovskite materials have attracted considerable attention as a class of functional advance materials in the mixed oxide family due to their structurally stable crystal lattice, high oxide ion conductivity, presence of oxygen vacancies, and excellent thermal and chemical stability. In recent years, perovskites have garnered significant interest due to their promising applications in catalysis,[1,2] electrocatalysis,[3] photocatalysis,[4] supercapacitors,[5] fuel cell electrodes,[2,5] metal–air batteries,[6] solar cells,[2,5,7] high density data storage devices,[8] magnetic memory devices,[9] separation membranes,[10] and sensors.[2] Perovskite materials typically adopt the general chemical formula of ABO_3, where A and B represent cations and 'O' denotes the oxygen anion. The A-site cation is usually an alkali metal, alkaline earth metal, or lanthanide, while the B-site cation is a transition metal with a 3d, 4d, or 5d electronic configuration. Partial substitution at the A and/or B sites enables tuning of the valence states of the cations and allows for the introduction of nonstoichiometry *via* cationic or anionic vacancies to maintain the overall charge neutrality. The remarkable multifunctional properties of perovskites are primarily attributed to their non-stoichiometry in both cationic and anionic sublattices, the presence of multiple oxidation states of metal ions, and structural distortions in the cation coordination environment.[2] Researchers have identified advanced functional properties in modified perovskites, which were achieved by converting simple perovskite structures into more complex forms, such as double perovskites, thereby enhancing their overall performance and application potential. Double perovskites, which are commonly represented by the empirical formula $A_2BB'O_6$, are an extension of the traditional ABO_3 perovskite structure. In this configuration, both the A-site and B-site cations serve as tunable host positions, providing a broad platform for structural and functional tuning across a wide range of applications. The incorporation of rare earth elements, alkali metals, and alkaline earth metals at the cationic sites of ordered double perovskites has led to significant enhancements in their

Materials Research Laboratory, Department of Physics, Banaras Hindu University (BHU), Varanasi 221005, India. E-mail: akghosh@bhu.ac.in, anupkg66@gmail.com

structural, electronic, and functional properties.[11,12] A-site cation substitutions significantly enhance the electrical, magnetic, optical, and dielectric properties of perovskites, as observed in $NaLaMgWO_6$,[13] $CaMnFeNbO_6$,[14] *etc.* Similarly, B-site substitution and doping, such as Bi_2FeMnO_6,[15] La_2NiMnO_6,[16] and La_2FeMnO_6,[17] perovskites have also attracted attention owing to their incredible physical properties.

Materials exhibiting high dielectric constants have attracted renewed interest over the past several decades due to their widespread applications in devices such as microwave filters, dynamic random-access memory, voltage-controlled oscillators, and telecommunication systems.[18,19] Lead-containing dielectric and ferroelectric materials are highly toxic and environmentally harmful. Consequently, the development of lead-free materials with rich dielectric characteristics is the major requirement at present. In last few years, significant research has been dedicated to developing lead-free materials with high dielectric constants.[17,19–22] Double perovskite materials have been extensively studied because of their diverse physical properties and potential for various multifunctional applications.[17,22,23] The charge conduction and relaxation behavior in rare-earth-based polycrystalline perovskites are significantly affected by temperature. To ensure an efficient performance in electronic and energy storage devices, various electrical parameters must be carefully optimized across a broad range of frequencies and temperatures. La-based compounds with the general formula $LaBO_3$ (where, B = Fe, Mn, Ni, Co, Cr, Sr, Al, *etc.*)[24–26] have attracted significant attention due to their distinct catalytic,[1,24,25] electrocatalytic,[3,26] photocatalytic,[4] magnetic,[27–29] optical,[27–29] electrical,[27,29] and sensing[28] properties. These properties are strongly dependent on parameters such as crystallinity, phase purity, particle size, and morphological characteristics. Additionally, the doping of metal ions with the +2 or +3 oxidation state into the $LaBO_3$ lattice significantly influences their structural and other functional properties.[24,27] In our earlier publication, an La_2FeMnO_6 (LFMO) double perovskite was successfully synthesized by the substitution of Mn into the Fe site of the $LaFeO_3$ single perovskite using the solid-state reaction method. This method was chosen due to its cost-effectiveness, minimal instrumentation requirements, and ability to yield materials with high crystallinity, phase purity, and chemical homogeneity. Further, we also studied its physical properties, which make it suitable for various multifunctional potential applications.[17] It exhibits a high dielectric constant (in the order of 10^3) accompanied by low energy loss at room temperature (RT). LFMO shows rich magnetic characteristics such as exchange bias, high Curie temperature, glassy transitions, and Griffiths phase due to disordering of FeO_6 and MnO_6 octahedra.[30–32] Based on the above-discussed characteristics, it can be used in energy storage capacitor and spintronic devices.

The doping of alkaline earth metals and transition metals into the A and B sites of the $LaFeO_3$ perovskite lattice has a remarkable impact on its electrical, dielectric, and magnetic properties.[17,27,33,34] Recently, many experimental studies have been reported on the effect of Sr doping on the physical and physicochemical properties of perovskite materials.[16,35–39] M. Qu *et al.*[16] reported that the electronic structure of $La_{2-x}Sr_x$-$NiMnO_6$ ($0 \leq x \leq 1.0$) can be effectively tuned to enhance its oxygen evolution reaction (OER) and oxygen reduction reaction (ORR) activities, facilitating the development of efficient bifunctional electrocatalysts. D. Chen *et al.*[35] reported that Sr doping is an effective strategy for enhancing the performance of perovskite light-emitting diodes (PeLEDs). Z. Wei *et al.*[36] reported that the introduction of Sr into $La_{0.5}Gd_{0.5}$-$Ba_{1-x}Sr_xCo_2O_{5+\delta}$ significantly enhances its performance as a cathode material for solid oxide fuel cell (SOFC) applications. M. Lamhani *et al.*[37] synthesized the $Ca_{1-x}Sr_xMnO_{3-\delta}$ ($0 \leq x \leq 1$) compound and observed a structural transition from an orthorhombic phase (*Pnma*) to a hexagonal phase (*P*63/*mmc*) within the composition range of $0.50 < x \leq 0.75$, while for $x = 0.50$, this material exhibited a mixed-phase structure of both orthorhombic (*Pnma*) and hexagonal (*P*63/*mmc*) symmetries. Moreover, the incorporation of strontium dopants has led to an improvement in the thermoelectric power factor, and a significant reduction in electrical resistivity. K. Sultan *et al.*[38] observed a decrease in the dielectric constant of $Pr_{2-x}Sr_xNiMnO_6$ (where, x = 0.0, 0.2, 0.4) with an increase in Sr concentration. N. Saadon *et al.*[23] observed a reduction in the band gap energy of $Sr_{2-x}Ca_xNiWO_6$ (where, x = 0.00, 0.02, 0.04, 0.06) with an increase in Sr concentration as well as an increase in its dielectric constant (at low frequencies). S. Abass *et al.*[39] reported that the degree of cationic disorder increases in $Nd_{2-x}Sr_xNiMnO_6$ (where, x = 0.0, 0.1, 0.3) with an increase in Sr concentration, resulting in an increase in its dielectric constant. T. Katheriya *et al.*[40] reported that the Sr doping at the La-site effectively modulated the negative permittivity of La_2NiO_4.

Motivated by these previous studies, the present work investigates the effect of Sr^{2+} substitution at the A-site of the La_2FeMnO_6 double perovskite (DP) on its structural, dielectric, magnetic, and electrical transport properties. To the best of our knowledge, no prior studies have explored the impact of Sr substitution at the La-site on these properties of La_2FeMnO_6 DP. A series of $La_{2-x}Sr_xFeMnO_6$ (where x = 0.0, 0.1, 0.2, 0.5, 0.1, 1.5 and 2.0) compounds was synthesized *via* the standard solid-state reaction method without the presence of any impurity phases, and also observed to show a re-entrant cubic–rhombohedral–cubic structural phase transition. Further, other physical properties (dielectric, magnetic, and electrical transport) were studied to determine the potential of this series for application in electronic devices.

2. Experimental details

2.1 Synthesis method

A polycrystalline series of $La_{2-x}Sr_xFeMnO_6$ (where x = 0.0, 0.1, 0.2, 0.5, 1.0, 1.5, 2.0) compounds was synthesized using the standard solid-state reaction method.[17,34] We employed high-purity La_2O_3 (purity 99.9%, HI media), $SrCO_3$ (purity 99%, HI media), Fe_2O_3 (purity 98%, HI media), and MnO_2 (purity 99%,

HI media) chemicals as precursors according to their stoichiometry and ground using an agate mortar for 3 h. The ground powder was heated to 1200 °C at a rate of 5 °C per minute and held at 1200 °C for 24 h in a muffle furnace in an air atmosphere, and then allowed to cool to RT naturally. The obtained powder was reground and calcined at 1200 °C for 7 h. Then, the calcined powder was ground again to get a fine powder. The obtained fine powder was uniaxially pressed into 10 mm dies to make pellets using a hydraulic press at a pressure of 12 bar. The obtained pellets were sintered at 1250 °C for 5 h in air to make them hard for further measurements. The chemical reaction is expressed by the following equation:

$$2(2-x)La_2O_3 + 4xSrCo_3 + 2Fe_2O_3 + 4MnO_2 \rightarrow 4La_{2-x}Sr_xFeMnO_6 + 4xCO_2(\uparrow) + (1-x)O_2(\uparrow)$$

2.2 Characterization techniques

X-ray powder diffraction (XRD) patterns were recorded at RT to analyze the structural properties of the synthesized samples using Cu Kα radiation (λ = 1.5406 Å) (Model: Empyrean, Malvern Panalytical, UK). The detailed structural information of the prepared samples was obtained through Rietveld refinement of the XRD data using the Full Prof Suite software. Surface morphology and elemental analysis were investigated using a field emission scanning electron microscope (FESEM) (Model: Gemini 560, Carl Zeiss, Germany) with an attached EDS unit. Raman spectra were collected at RT using a Raman spectrometer (Model: WITec Alpha 300 RA, Germany) with an excitation source wavelength of 532 nm. Fourier transmission infrared (FT-IR) spectra were recorded in KBr mode at RT using an FT-IR spectrometer (Spectrum One, PerkinElmer Instrument, USA) with a resolution of 1 cm^{-1}. X-ray photoelectron spectroscopy (XPS) measurements were performed to study the electronic structure using a monochromatic Al Kα X-ray source (1486.6 eV) with an energy resolution of 1 eV (Instrument model: PHI 5000 Versa Probe III, Japan). The setup included a pass energy of 100 eV, an R4000 VG Scientia analyzer, and an X-ray source operating at 450 W. The pressure inside the chamber was maintained at 4.48×10^{-10} mbar. Both sides of the pellet were polished uniformly with high quality conducting silver paste (Sigma Aldrich) for electrical measurements. Room temperature dielectric and impedance measurements were carried out using a LCR meter (Model: E4980A Precision, Agilent, USA) across the frequency range of 100 Hz to 2 MHz. Temperature-dependent DC resistivity and current–voltage (I–V) measurements were conducted using a source meter (Model: 2634B, Keithley, USA). Room temperature magnetic hysteresis loops were recorded using a vibrational sample magnetometer (VSM) (Model: EZ9, Microsense, USA).

3. Results and discussion

3.1 Structural analysis

Fig. 1(a) shows the XRD patterns of $La_{2-x}Sr_xFeMnO_6$ (where x = 0.0, 0.1, 0.2, 0.5, 0.1, 1.5 and 2.0) solid solutions at RT. The presence of sharp and many distinct diffraction peaks indicates their polycrystalline bulk nature. The diffraction peaks were indexed based on the JCPDS file (JCPDS Card # 01-078-4452) corresponding to the cubic phase with $Pm\bar{3}m$ space group. The XRD pattern of the undoped sample (x = 0.0) matched well with

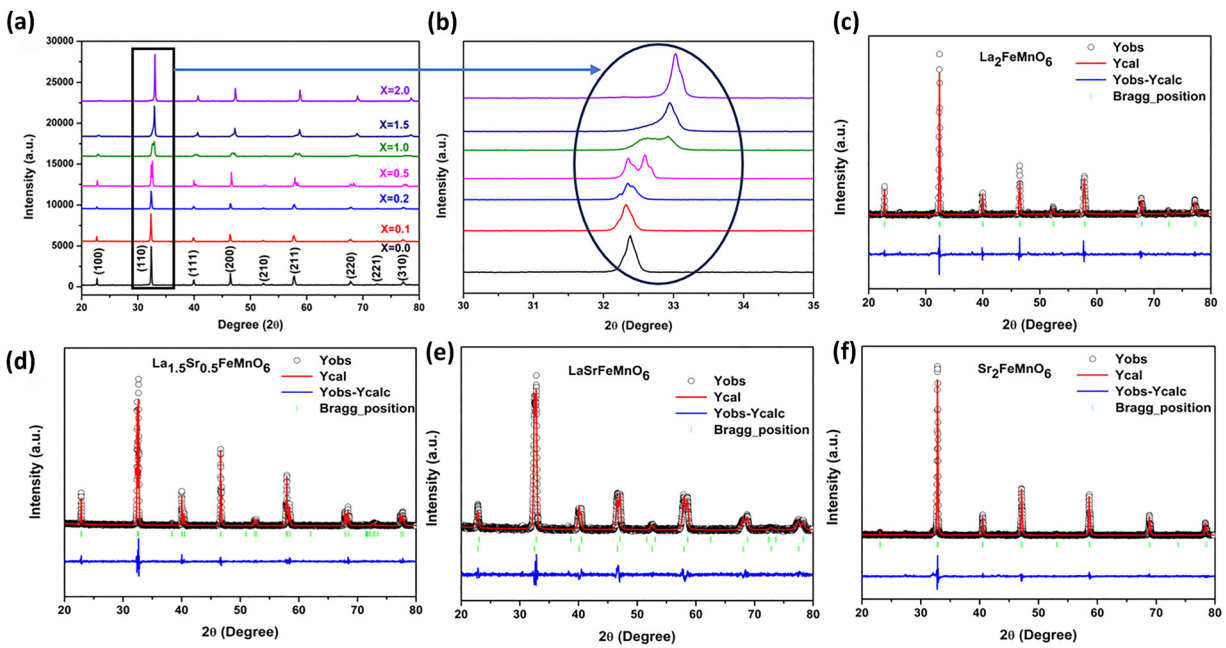

Fig. 1 (a) X-ray diffraction patterns of $La_{2-x}Sr_xFeMnO_6$ (where x = 0.0, 0.1, 0.2, 0.5, 1.0, 1.5, and 2.0) and (b) enlarged view of the most intense peak corresponding to the (110) plane. (c)–(f) Rietveld refinement for the x = 0.0, 0.5, 1.0, and 2.0 samples, respectively.

our earlier reported results.[17,34] No impurity peak was observed for the synthesized samples within the detection limits of XRD analysis, demonstrating the high purity of the materials. Fig. 1(b) shows a magnified view of the diffraction peak positioned in the 2θ range of 32.2–33.10°. According to this figure, it can be observed that as the concentration of Sr^{2+} dopant increased, the diffraction peaks shifted towards lower 2θ values up to $x = 0.2$, and after that they split and shifted to the higher angle side. This splitting and shifting indicate a change in the phase and unit cell parameters, respectively. These changes are attributed to the substitution of the Sr^{2+} bivalent cation ($r = 1.44$ Å) for the trivalent La^{3+} cation ($r = 1.36$ Å) at the A-site of the LFMO compound. The XRD patterns for the $x = 0.0$, 0.1 and 0.2 samples show their cubic (single phase) perovskite structure. Further, in the case of the $x = 0.5$ and 1.0 samples, the most intense peak located at $2\theta \sim 32.3°$ split, which indicates that the symmetry of their crystal structure deviates from cubic. To gain a better understanding of the crystal structural of LSFMO, the experimental XRD patterns were refined through Rietveld refinement using the FULLPROF suite software with their appropriate phase along with space group, as shown in Fig. 1(c)–(f) for some selected samples ($x = 0.0$, 0.5, 1.0 and 0.2), respectively. The strong correlation between the experimental and calculated XRD patterns, along with the low value of the *R*-factors and χ^2, indicates the good quality of the refinement. During the refinement process, careful attention was given to multiple parameters, including background correction, zero shift, sample displacement, atomic coordinates, thermal vibration factors, scale factor, lattice constants, FWHM, and peak shape parameters. The XRD patterns of the $x = 0.0$, 0.1, and 0.2 compositions were successfully refined with a disordered cubic structure ($Pm\bar{3}m$), while for $x = 0.5$, it is refined well with a disordered rhombohedral structure ($R\bar{3}c$). Further, for the $x = 1.0$ and 1.5 compositions, the refinement shows the mixed contribution of both disordered cubic ($Pm\bar{3}m$) and disordered rhombohedral ($R\bar{3}c$) phases. Furthermore, for $x = 2.0$, its XRD pattern was refined well with the cubic ($Pm\bar{3}m$) phases. Hence, it can be concluded that LFMO shows a re-entrant structural phase transition (cubic-rhombohedral-cubic) with Sr doping (substitution). The fractional atomic coordinates, occupancy, and other structural parameters of the $La_{2-x}Sr_xFeMnO_6$ (where $x = 0.0$, 0.1, 0.2, 1.5, and 2.0) compounds obtained from the Rietveld refinement are given in Table 1. Prior to this study, a lot of research has been done on A-site doped perovskites but it is limited to partial substitution.[16,36,37,41] They observed various phase transitions but not a re-entrant structural phase transition. M. Qu *et al.*[16] reported that the $La_{2-x}Sr_xNiMnO_6$ ($0 \leq x \leq 1.0$) perovskite crystallize into a rhombohedral structure with $R\bar{3}c$ symmetry, and a secondary phase was observed as rocksalt NiO, when the amount of Sr doping was $x \geq 0.8$. Z. Wei *et al.*[36] synthesized the $La_{0.5}Gd_{0.5}Ba_{1-x}Sr_xCo_2O_{5+\delta}$ ($LGBCOS_{r-x}$, $x = 0$–0.5) perovskite *via* the solid state reaction route and reported a structural phase transition from a double layered tetragonal phase to a single layered cubic phase with an increase in the Sr doping ratio. J. K. Murthy *et al.*[41] observed a structural phase transition in $La_{2-x}Sr_xCoMnO_6$ ($0 \leq x \leq 1.0$) double perovskite from monoclinic to disordered rhombohedral ($R\bar{3}c$) to mixed phase of disordered rhombohedral ($R\bar{3}c$) and cubic ($Fm\bar{3}m$) symmetry with an increase in Sr amount. Moreover, for $x > 1$, they observed some impurity peaks corresponding to the Co_3O_4 and MnO_2 phases.

The Visualization of Electronic and Structural Analysis (VESTA) software was used to illustrate the unit cell structures utilizing the structural parameters obtained by the Rietveld refinement. Fig. 2(a)–(c) display the unit cell crystal structures of some selected samples with compositional $x = 0$, 0.5, and 2.0. The bond length and bond angle values between the Fe/Mn ions and oxygen atoms in the surrounding area of the octahedral coordination are determined using the bond structure program of Full Prof Suite software, as listed in Table 1. The tolerance factor (t) gives a basic idea about the single-phase formation, structural stability, and structural imperfection of perovskites. The tolerance factor for the $La_{2-x}Sr_xFeMnO_6$ compounds was calculated using the following expression:[34,42]

$$T_f = \frac{\left(1-\frac{x}{2}\right)R_{La} + \frac{x}{2}R_{Sr} + R_O}{\sqrt{2}\left(\frac{R_{Fe}+R_{Mn}}{2} + R_O\right)} \quad (1)$$

where, R_{La} is the ionic radius of La, R_{Sr} is the ionic radius of Sr, R_{Fe} is the ionic radius of Fe, R_{Mn} is the ionic radius of Mn, and R_O is the ionic radius of O. These values are as follows: $R_{La^{3+}}$ = 1.36 Å; $R_{Sr^{2+}}$ = 1.44 Å; $R_{Mn^{3+}}$ = (HS: 0.65 Å, LS: 0.58 Å); $R_{Fe^{3+}}$ = (HS: 0.65 Å, LS: 0.55 Å); and $R_{O^{2-}}$ = 1.35 Å. The tolerance factor typically lies between 0.75 to 1.02 for a stable perovskite structure. If $T_f = 1$, perovskites adopt an ideal cubic structure. In this study, the tolerance factor was obtained in the range of 0.977 to 1.006 (as given in Table 2), which is close to 1, supporting the cubic symmetry of the samples. The change in T_f with Sr substitution is attributed to the difference in ionic radii between the La^{3+} and Sr^{2+} cations, which indicates their good structural stability.

The crystallite size (D) and lattice micro strain (ε) were calculated from the XRD data of the synthesized samples. Various methods are available to calculate these parameters such as Williamson–Hall (W–H) analysis, pseudo-Voigt function, and Warren–Averbach analysis, considering the effect of the strain-induced XRD peak broadening, and accurately estimate the crystallite size along with the intrinsic strain. Among them, the W–H method for the analysis is generally used to distinguish the XRD peak broadening induced by crystallite size and microstrain.[43] In this model, line broadening induced by crystallite size and micro strain contributes independently to the total integral breadth of the full-width-at-half maximum (FWHM) of a diffraction peak. According to this model, a uniform micro-strain develops in all crystallographic directions. The FWHM of the Bragg peak is the addition of broadening induced by both the crystallite size and the micro strain, which is expressed as follows:

$$\beta_{hkl} = \beta_{\text{crystallite size}} + \beta_{\text{microstrain}} \quad (2)$$

Table 1 Structural parameters obtained from the Rietveld refinement of the $La_{2-x}Sr_xFeMnO_6$ (where x = 0.0, 0.1, 0.2, 0.5, 1.0, 1.5, and 2.0) DPs

Crystallographic parameters	x = 0.0	x = 0.1	x = 0.2	x = 0.5	x = 1.0	x = 1.5	x = 2.0
Crystal structure	Cubic	Cubic	Cubic	Rhombohedral	Rhombohedral + Cubic	Rhombohedral + Cubic	Cubic
Space group	$Pm\bar{3}m$	$Pm\bar{3}m$	$Pm\bar{3}m$	$R\bar{3}c$	$R\bar{3}c$ (42%) + $Pm\bar{3}m$ (58%)	$R\bar{3}c$ (14%) + $Pm\bar{3}m$ (86%)	$Pm\bar{3}m$
Lattice parameters							
a (Å)	$3.9065 \pm 8.0 \times 10^{-4}$	$3.9080 \pm 7.8 \times 10^{-4}$	$3.9056 \pm 8.2 \times 10^{-4}$	$5.5218 \pm 7.5 \times 10^{-4}$	$(5.4602 \pm 6.9 \times 10^{-4}) + (3.8962 \pm 7.5 \times 10^{-4})$	$(5.5216 \pm 7.2 \times 10^{-4}) + (3.8541 \pm 8.1 \times 10^{-4})$	$3.8552 \pm 6.4 \times 10^{-4}$
b (Å)	$3.9065 \pm 8.0 \times 10^{-4}$	$3.9080 \pm 7.8 \times 10^{-4}$	$3.9056 \pm 8.2 \times 10^{-4}$	$5.5218 \pm 7.5 \times 10^{-4}$	$(5.4602 \pm 6.9 \times 10^{-4}) + (3.8962 \pm 7.5 \times 10^{-4})$	$(5.5216 \pm 7.2 \times 10^{-4}) + (3.8541 \pm 8.1 \times 10^{-4})$	$3.8552 \pm 6.4 \times 10^{-4}$
c (Å)	$3.9065 \pm 8.0 \times 10^{-4}$	$3.9080 \pm 7.8 \times 10^{-4}$	$3.9056 \pm 8.2 \times 10^{-4}$	$13.3837 \pm 8.4 \times 10^{-4}$	$(13.3718 \pm 8.1 \times 10^{-4}) + (3.8962 \pm 7.5 \times 10^{-4})$	$(13.3837 \pm 7.2 \times 10^{-4}) + (3.8541 \pm 8.1 \times 10^{-4})$	$3.8552 \pm 6.4 \times 10^{-4}$
V (Å^3)	$59.616 \pm 3.67 \times 10^{-2}$	$59.683 \pm 3.75 \times 10^{-2}$	$59.574 \pm 3.84 \times 10^{-2}$	$353.40 \pm 10.9 \times 10^{-2}$	$(345.25 \pm 10.1 \times 10^{-2}) + (59.14 \pm 4.0 \times 10^{-2})$	$(353.37 \pm 8.7 \times 10^{-2}) + (57.24 \pm 4.0 \times 10^{-2})$	$57.30 \pm 2.67 \times 10^{-2}$
α, β, and γ (°)	$\alpha = \beta = \gamma = 90$	$\alpha = \beta = \gamma = 90$	$\alpha = \beta = \gamma = 90$	$\alpha = \beta = 90$ and $\gamma = 120$	$\alpha = \beta = 90$ & $\gamma = 120$ + $\alpha = \beta = \gamma = 90$	$\alpha = \beta = 90$ & $\gamma = 120$ + $\alpha = \beta = \gamma = 90$	$\alpha = \beta = \gamma = 90$
Atomic position							
La/Sr							
x	0.00	0.00	0.00	0.00	0.00 + 0.00	0.00 + 0.00	0.00
y	0.00	0.00	0.00	0.00	0.00 + 0.00	0.00 + 0.00	0.00
z	0.00	0.00	0.00	0.25	0.25 + 0.00	0.25 + 0.00	0.00
Occupancy	1.0/0.0	0.95/0.05	0.90/0.10	0.72/0.22	0.50/0.50 + 0.52/0.50	0.27/0.73 + 0.25/0.75	0.0/0.1
Mn/Fe							
x	0.50	0.50	0.50	0.00	0.00 + 0.50	0.00 + 0.50	0.50
y	0.50	0.50	0.50	0.00	0.00 + 0.50	0.00 + 0.50	0.50
z	0.50	0.50	0.50	0.00	0.00 + 0.50	0.00 + 0.50	0.50
Occupancy	0.53/0.50	0.40/0.66	0.50/0.50	0.50/0.48	0.50/0.50 + 0.46/0.50	0.48/0.50 + 0.50/0.50	0.5/0.5
O							
x	0.50	0.50	0.50	0.46015	−0.48 + 0.50	0.45 + 0.50	0.50
y	0.50	0.50	0.50	0.00	0.00 + 0.50	0.00 + 0.50	0.50
z	0.00	0.00	0.00	0.25	0.25 + 0.00	0.25 + 0.00	0.00
Occupancy	2.79	2.97	3.0	2.98	2.44 + 2.31	3.09 + 3.00	2.95
R factors (%)							
R_p	5.95 ± 0.62	9.22 ± 0.57	10.3 ± 0.64	7.69 ± 0.54	6.98 ± 0.67	6.78 ± 0.72	6.50 ± 0.56
R_{wp}	8.19 ± 0.68	12.3 ± 0.62	13.6 ± 0.67	9.80 ± 0.56	8.76 ± 0.71	8.49 ± 0.75	8.41 ± 0.48
R_{exp}	6.19 ± 0.64	10.3 ± 0.58	11.8 ± 0.62	9.45 ± 0.52	8.73 ± 0.65	8.04 ± 0.69	7.25 ± 0.44
χ^2	1.75 ± 0.40	1.45 ± 0.21	1.33 ± 0.30	1.07 ± 0.27	1.01 ± 0.36	1.11 ± 0.23	1.34 ± 0.18
Bond length (Å)							
La/Sr–O	2.7628	2.7633	2.7616	2.4987(2), 3.0230(3), 2.7541(8)	—	—	2.7260
Mn/Fe–O	1.9536	1.9539	1.9548	1.9330	1.9345	2.7588	1.9275
Bond angle (°)							
Fe–O–Fe	180	180	180	164.65	172.44 + 180	180	180
Fe–O–Mn	180	180	180	164.65	172.44 + 180	180	180
Mn O–Mn	180	180	180	164.65	172.44 + 180	180	180
La/Sr–O–Fe/Mn	90	90	90	—	—	90	90

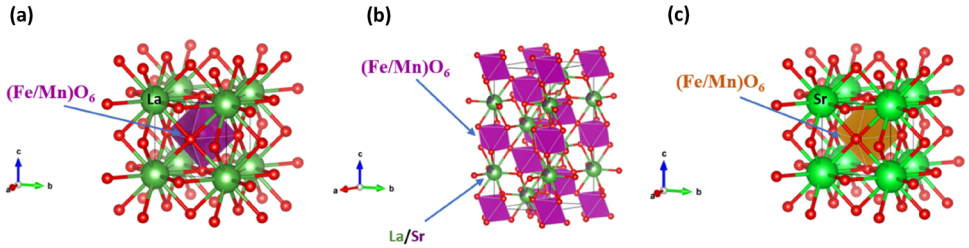

Fig. 2 (a)–(c) Unit cell of the crystal lattice of $La_{2-x}Sr_xFeMnO_6$ for x = 0, 0.5 and 2.0, respectively.

The broadening of the diffraction peaks induced by the crystallite size is written as follows:

$$\beta_{\text{crystallite}} = \frac{K\lambda}{D\cos\theta} \quad (3)$$

where $K = 0.94$ is a constant for a spherical-shaped particle, λ is the wavelength of X-ray radiation (0.15406 nm for Cu Kα radiation), D is the crystallite size, and θ is the Bragg angle. The broadening of the diffraction peaks induced by the microstrain is expressed as follows:

$$\beta_{\text{microstrain}} = 4\varepsilon\tan\theta \quad (4)$$

Using eqn (2)–(4), the total broadening of diffraction peak can be expressed as:

$$\beta_{hkl} = \frac{K\lambda}{D\cos\theta} + 4\varepsilon\tan\theta \quad (5)$$

Rearranging eqn (5), we get eqn (6), which is known as the uniform deformation model (UDM) equation.

$$\beta_{hkl}\cos\theta = \frac{K\lambda}{D} + 4\varepsilon\sin\theta \quad (6)$$

A plot is drawn with $(4\sin\theta)$ along the X-axis and $(\beta_{hkl}\cos\theta)$ along the Y-axis using values obtained from each diffraction peak of the XRD pattern. In this case, β_{hkl} (FWHM in radians) for each diffraction peak was taken after subtracting the instrumental broadening (β_i) from the observed broadening (β_0),[34] which is an important step in the W–H analysis. The value of β_0 for each prominent XRD peak was obtained by peak fitting using the Gaussian function. The best linear fitting of these data points indicates a uniform deformation model. According to the resulting straight line, the crystallite size can be determined from the intercept at the Y-axis, and the slope of the resulting straight line provides the corresponding intrinsic micro strain. The average crystallite size of the prepared samples was estimated from the W–H method, which was found to be in the range of 49 to 354 nm, as given in Table 2. The value of intrinsic micro strain for all the synthesized samples is found in the range of 0.03×10^{-3} to 0.47×10^{-3}, which is also given in Table 2. Fig. 3(a)–(d) shows the W–H plot of $La_{2-x}Sr_xFeMnO_6$ DPs for some selected samples of x = 0.0, 0.5, 1.0, and 2.0.

The porosity of the synthesized samples in percentage (P%) was calculated using their X-ray and experimental densities based on the following relation:

$$P = \left(1 - \frac{d_{\text{expt}}}{d_{\text{X-ray}}}\right) \times 100\% \quad (7)$$

The value of P (%) for all the synthesized materials was found to be in the range of 46% to 83%, which are listed in Table 2. The smallest porosity (~46%) is observed for x = 0.5, while the highest porosity (~86%) is observed for the x = 1.5 sample. The X-ray or theoretical densities ($d_{\text{X-ray}}$) of all the synthesized samples were calculated using the following relation:

$$d_{\text{X-ray}} = \frac{ZM}{N_A V} \quad (8)$$

where Z represents the number of molecules per unit cell (Z = 2 for body-centered cubic structures and Z = 4 for rhombohedral structures), M is the molecular weight of the sample, N_A is Avogadro's number (6.023×10^{23} particles per mol), and V is the unit cell volume in cm^3. The experimental (measured) densities (d_{exp}) of all the synthesized materials were measured using their cylindrical pellets and the following equation:

$$d_{\text{expt}} = \frac{m}{V} = \frac{m}{\pi r^2 h} \quad (9)$$

where m, V, r, and h represent the mass, volume, radius, and thickness of the pellet, respectively. It is important to note that the X-ray density depends directly on the molecular weight and

Table 2 Tolerance factor, crystallite size, micro-strain, density and porosity of the $La_{2-x}Sr_xFeMnO_6$ (where x = 0.0, 0.1, 0.2, 0.5, 1.0, 1.5, and 2.0) samples

Concentration (x)	Tolerance factor (t)	Crystallite size (nm)		Micro-strain ($\times 10^{-3}$)		X-ray density (g cm^{-3})	Measured density (g cm^{-3})	Porosity ~(%)
		Cubic	Rhombohedral	Cubic	Rhombohedral			
x = 0.0	0.978	133	—	0.47	—	26.95	5.02	81.4
x = 0.1	0.979	152	—	0.41	—	26.61	4.87	81.7
x = 0.2	0.980	96	—	0.42	—	26.44	4.66	82.4
x = 0.5	0.984	—	185	—	0.13	08.63	4.64	46.2
x = 1.0	0.992	50	142	0.89	0.26	16.05	4.42	72.5
x = 1.5	0.999	49	354	0. 05	1. 03	13.68	3.25	76.2
x = 2.0	1.006	75	—	0.05	—	22.13	4.16	81.2

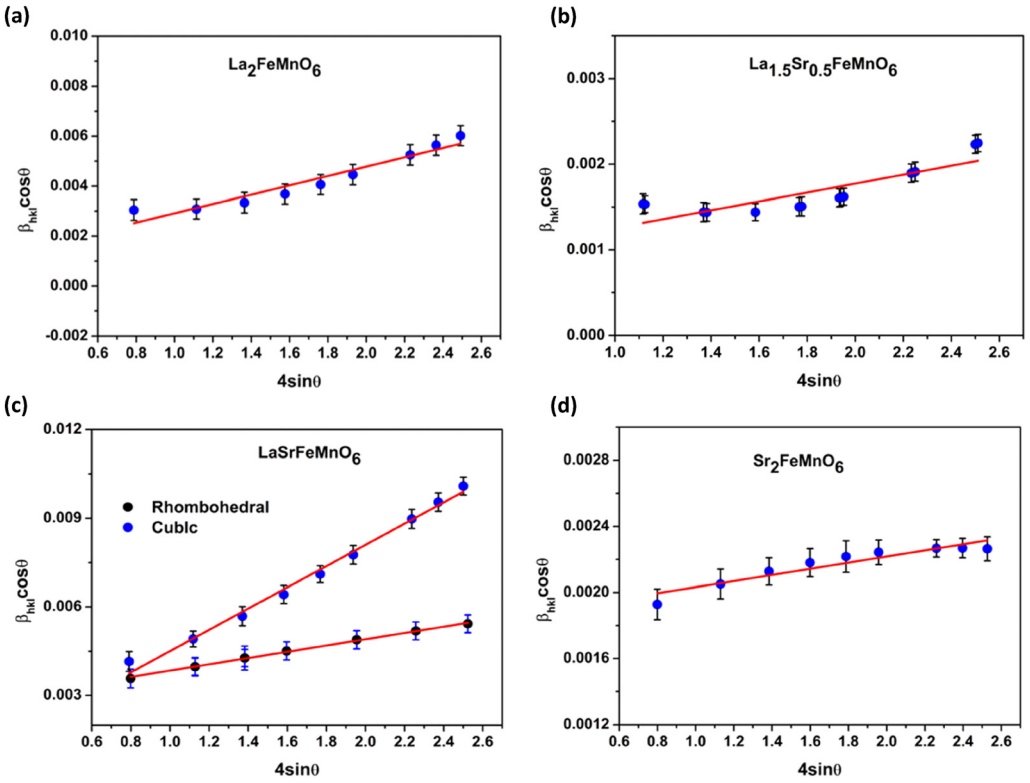

Fig. 3 Williamson–Hall plot for (a) La_2FeMnO_6 (x = 0.0), (b) $La_{1.5}Sr_{0.5}FeMnO_6$ (x = 0.5), (c) $LaSrFeMnO_6$ (x = 1.0), and (d) Sr_2FeMnO_6 (x = 2.0).

lattice parameters of the sample, while the experimental density is calculated from the mass and volume of the geometry of materials. The measured densities of all the synthesized materials are lower than their corresponding X-ray densities, primarily due to their porous nature resulting from the solid-state reaction (SSR) synthesis route. Both the theoretical and measured densities of all the synthesized materials are summarized in Table 2.

3.2 Surface and elemental analysis

The microstructure and surface morphology of the sintered pellets were examined using a field emission scanning electron microscope (FE-SEM). Fig. 4(a)–(c) show the SEM images of the cross-section area of the pellets after Au coating, showing 'stacked flake-like' grains. The average grain size was estimated from the grain size distribution histograms obtained from the FESEM micrographs using the ImageJ software. As illustrated in Fig. 4(d)–(f), the estimated average grain sizes for the samples with compositions x = 0.0, 0.2, and 0.5 are ~4 μm, 1.5 μm, and 0.2 μm, respectively. Generally, ideal cubic perovskites typically exhibit isotropic thermal expansion along each of their three axes because their crystal structure is symmetrical. However, in the case of the $La_{2-x}Sr_xFeMnO_6$ material, anisotropic thermal expansion is observed during grain formation, as shown in the inset of Fig. 4(a) and (b). This expansion contributes to the development of micro porosity.[44] A significant increase is observed in pore size with Sr substitution, reducing the structural density of the synthesized material. We also estimated the porosity of the sintered pellets at RT in the XRD section. The observed trend of porosity in the SEM micrographs with Sr substitution corroborates well with the porosity calculated using the XRD results. The EDAX spectra of the x = 0.0, 0.2, and 1.5 compositions reveal the presence of La, Sr, Mn, Fe, and O elements with their ideal atomic ratios, as shown in Fig. 4(g)–(i). The atomic and weight percentages of the elements present in the x = 0, 0.2, and 1.5 samples are listed in Table 3. The elemental percentages of these elements indicate a slight oxygen deficiency and a minor excess of La, Fe and Mn cations compared to their ideal stoichiometric ratios, indicating the presence of a very small amount of oxygen vacancies in the lattices. These results are corroborated by results obtained from the Rietveld refinement of the XRD data.

3.3 Raman analysis

Raman spectroscopy is a powerful technique for analyzing the lattice dynamics, vibrational modes, and atomic structure of materials. In the ideal cubic perovskite ABO_3, Raman-active modes are absent because all the atoms are occupied at centrosymmetric positions. However, deviation from cubic symmetry, primarily due to tilting of the BO_6 octahedra, introduces Raman activity. This tilting can be influenced by the ionic radius of the A-site cation, leading to structural distortions. Specifically, the movement of oxygen atoms within the BO_6 octahedra around the B-site atoms gives rise to Raman-active vibrational modes. The vibrational frequency of the

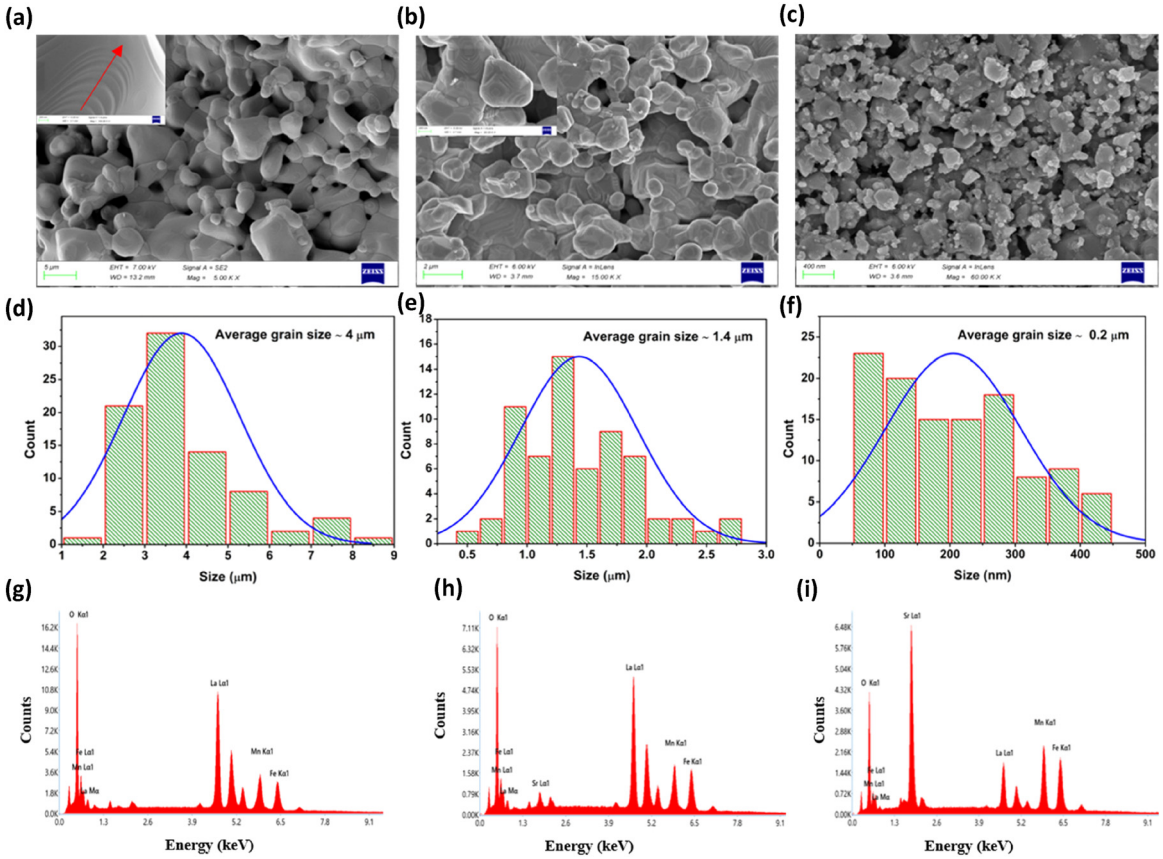

Fig. 4 (a)–(c) FESEM images, (d)–(f) corresponding grain size distribution histograms, and (g)–(i) EDS spectra of $La_{2-x}Sr_xFeMnO_6$ for x = 0.0, 0.2, and 1.5, respectively.

Table 3 Weight/atomic percentage (%) of the elements present in $La_{2-x}Sr_xFeMnO_6$ (where x = 0.0, 0.2, and 1.5) material

	x = 0.0		x = 0.2		x = 1.5	
Elements	Weight (%)	Atomic (%)	Weight (%)	Atomic (%)	Weight (%)	Atomic (%)
La L	58.8	20.1	55.3	19.9	20.7	6.6
Sr L	0.0	0.0	3.1	1.8	28.8	14.6
Fe K	10.0	8.5	12.0	10.7	14.4	11.5
Mn K	10.1	8.7	11.2	10.2	16.6	13.4
O K	21.1	62.6	18.4	57.4	19.5	54.0

Raman modes is influenced by both the bond length and the reduced mass of the vibrating system. As a result, the Raman lines for lighter cations and lower bond length between cations take place at the higher wavenumber side, and *vice versa*. The Raman spectra of the $La_{2-x}Sr_xFeMnO_6$ (where x = 0.0, 0.1, 0.2, 0.5, 1.0, 1.5, and 2.0) materials were recorded in the range of 100–3000 cm^{-1}, which are shown in Fig. 5. The recorded Raman spectra matched well with that previously reported in the literature.[17,31] Two prominent phonon modes were observed in the range of 485–502 cm^{-1} and 653–672 cm^{-1}, which are related to the anti-stretching and/or bending vibrations of the $(Fe/Mn)O_6$ octahedra with A_{1g} symmetry and the stretching ("breathing") vibrations of the $(Fe/Mn)O_6$ octahedra

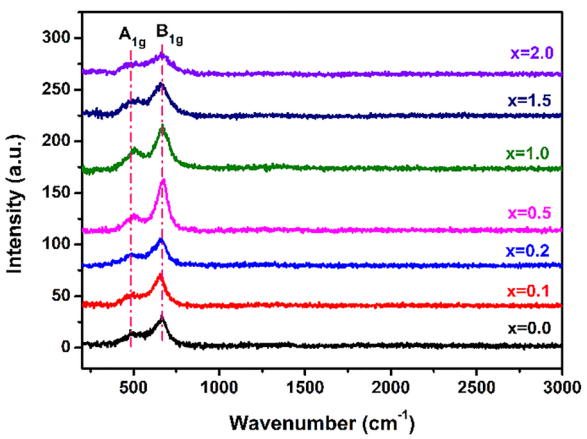

Fig. 5 Raman spectra of $La_{2-x}Sr_xFeMnO_6$ (where x = 0.0, 0.1, 0.2, 0.5, 1.0, 1.5, and 2.0).

with B_{1g} symmetry, respectively.[17,31,34,45] Sr doping changes the position and intensity of the peaks associated with the A_{1g} and B_{1g} Raman modes, which indicates the successful doping of Sr ions. The noticeable change in the Raman shift of both the A_{1g} and B_{1g} modes with Sr concentration is a result of the bond length of the Fe–O and Mn–O bonds. The highest peak

intensity of the Raman modes is observed for rhombohedral symmetry (x = 0.5), which indicates minimal distortion in the rhombohedral lattice. Further, the Raman peak intensity of each lattice phase (cubic and rhombohedral) decreases with an increase in the Sr substitution amount, leading to distortion in the lattice of La_2FeMnO_6 due to the mismatch in the ionic radii of La^{3+} (1.36 Å) and Sr^{2+} (1.44 Å) atoms.

3.4 X-ray photoemission spectroscopy (XPS) analysis

X-ray photoemission spectroscopy (XPS) is a powerful tool for studying the surface elemental composition, chemical and electronic structure of individual elements, empirical formula of doped and undoped samples, and their corresponding binding energy (BE). It is widely recognized for investigating the electronic characteristics of materials. In this technique, samples are irradiated with Al Kα X-rays ($h\nu$ = 1486.6 eV) and the kinetic energy of the emitted electrons is measured. The emitted photoelectron is the result of the complete transfer of incident energy ($h\nu$) to a core-level electron. This can be expressed mathematically as follows:

$$h\nu = \mathrm{BE} + \mathrm{KE} + \Phi_{\mathrm{spec}} \quad (10)$$

where $h\nu$ is the energy of the Al Kα X-rays; BE is the energy that binds an electron tightly with the atom/orbital, which is called the binding energy; KE is the kinetic energy of the emitted photo electrons and Φ_{spec} is the work function of the spectrometer, which is constant for the instrument used. The photoelectron binding energy is measured with respect to the Fermi level of the sample (not the vacuum level), which is why Φ_{spec} is included. The BE of an electron is a material property and is independent of the X-ray source used to eject it, while KE changes for different X-ray sources. This concept is demonstrated by a simple schematic energy level diagram in Fig. 6. Hence, the oxidation states of the elements present in materials have been identified by the BE of an ejected electron, where the BE is determined using eqn (10). The XPS spectra of the x = 0.0, 0.5, and 2.0 samples were recorded to learn about their electronic structure. The XPS database hosted by the National Institute of Standards and Technology (NIST) was used to calibrate the peak positions and doublet separations in all the recorded XPS spectra. The XPS survey scan spectra reveal that La, Mn, Fe, and O elements are present in all the measured samples, while Sr is present in both the x = 0.5 and x = 2.0 samples, as shown in Fig. 7(a). We set the C 1s peak (adsorbed from air on the surface) at 284.8 eV in the survey scan spectrum as the reference energy.

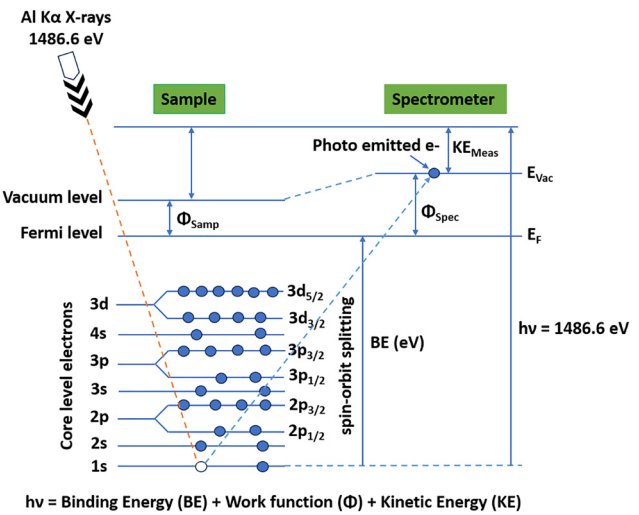

Fig. 6 Schematic of the energy level diagram for charge hopping in the XPS technique.

Fig. 7(b) displays the core-level XPS spectra of La 3d for the x = 0.0 and 0.5 samples. The spin–orbit split peaks associated with La $3d_{3/2}$ and La $3d_{5/2}$ appear in a binding energy in the range of 850.3–851.2 eV and 833.7–834 eV, respectively. The separation energy (ΔE) of the La $3d_{3/2}$–La $3d_{5/2}$ spin–orbit split is obtained in the range of 16.6–17.2 eV. Besides these peaks, other binding energy peaks are also observed in all the measured samples. The La $3d_{3/2}$–La $3d_{5/2}$ spin–orbit split is attributed to the excitation of an electron coming from the O 2p valence band and transferred into the unoccupied La 4f orbital, which is associated with the other observed peaks (La 3d shake-up state).[46] The ΔE value for the La $3d_{3/2}$–La $3d_{5/2}$ spin–orbit is reported in the range of 16.6–16.9 eV, indicating the La^{3+} oxidation state.[47] Thus, the observed features reveal that the La ion exists in the La^{3+} oxidation state.

Fig. 7(c) displays the core-level XPS spectra of the Sr 3d for x = 0.5 and 2.0 samples. The spin–orbit split Sr $3d_{3/2}$–Sr $3d_{5/2}$ peaks are observed in the range of 132.9–134.5 eV and 131.1–132.6 eV for Sr $3d_{3/2}$ and Sr $3d_{5/2}$, respectively. The doublet separation energy (ΔE) for this splitting is found in the range of 1.7–2.0 eV, indicating the Sr^{2+} oxidation state.[48,49] Another peak is observed in the range of 132.6–134.1 eV, which originates from the Sr–OH, Sr–CO_3, Sr–Sr, and Sr–O bonds on the surface area of the materials.[49]

Fig. 7(d) represents the Fe 2p core-level XPS spectra of the x = 0.0, 0.5, and 2.0 samples. They consist of 4 peaks at x = 0, while 3 peaks are observed in the Sr-doped x = 0.5 and x = 2.0 samples. The peaks positioned in the range of 709.4–710.4 eV and 723.1–724.4 eV are related to Fe $2p_{3/2}$ and Fe $2p_{1/2}$, respectively, which are associated with the Fe^{3+} oxidation state.[46] In the case of the Fe $2p_{3/2}$–Fe $2p_{1/2}$ spin–orbit split, the value of ΔE was obtained in the range of 13.7–14.0 eV. For this spin–orbit split, the value of ΔE is reported to be ~13.7 eV, which is associated with the Fe^{3+} oxidation state.[50] In addition, the other peak observed in the range of 711.9–713.1 eV is ascribed to the Fe^{4+} oxidation state, which is related to the creation of La vacancies.[51] All these observations indicate the presence of mixed Fe^{3+} and Fe^{4+} oxidation states. The deconvolution analysis of the Fe 2p core-level XPS spectra shows an increment in the percentage of Fe^{3+} (52% for x = 0 to 88% for x = 0.5) oxidation state and decrease in Fe^{4+} (48% for x = 0 to 12% for x = 0.5) with Sr^{2+} substitution, which was predicted earlier, because the system would essentially attempt to preserve charge neutrality. In addition, a prominent charge transfer satellite peak is observed between the main Fe 2p split peaks

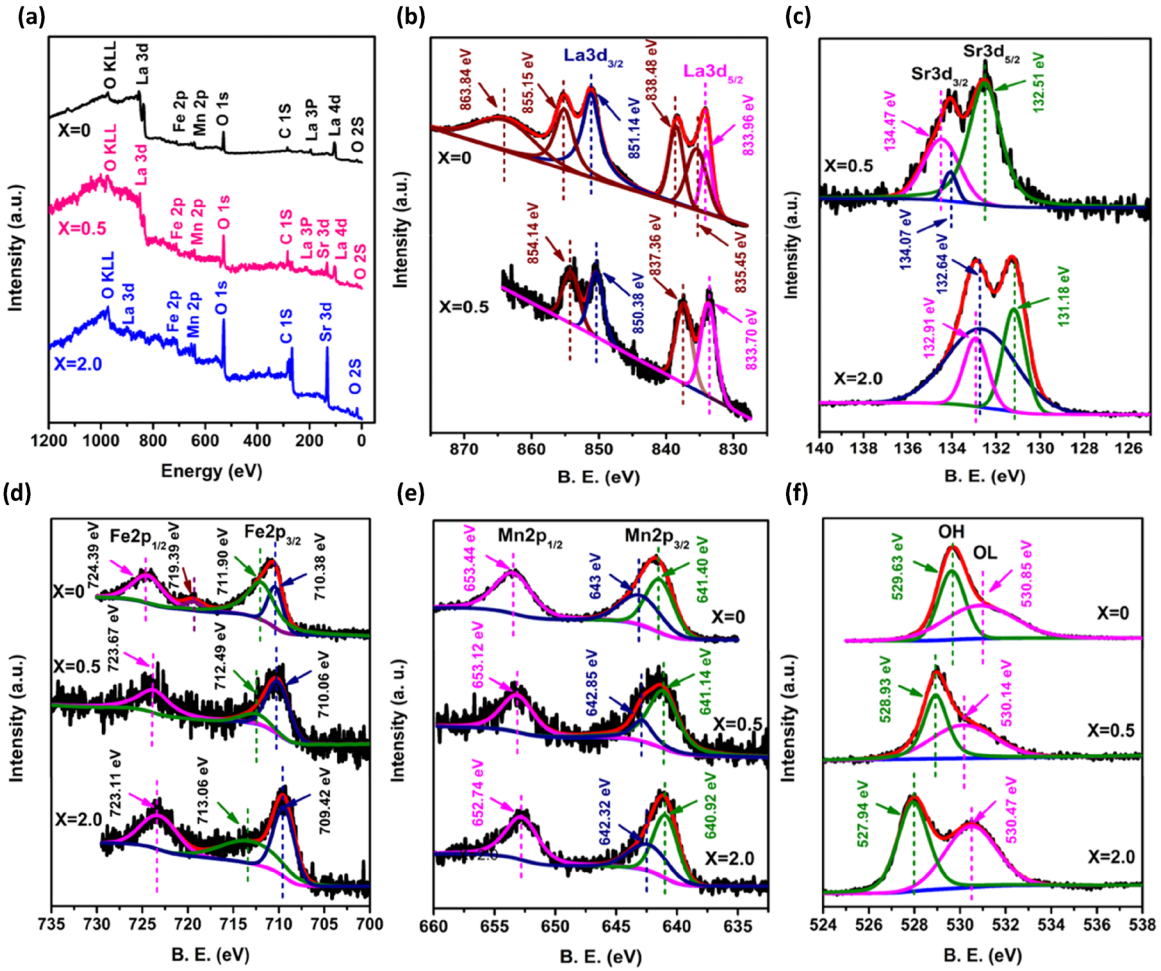

Fig. 7 (a) XPS survey scan; core-level spectra of (b) La 3d, (c) Sr 3d, (d) Fe 2p, (e) Mn 2p, and (f) O 1s for $La_{2-x}Sr_xFeMnO_6$ with x = 0.0, 0.5, and 2.0 compositions.

at ~719.4 eV, which appears very weak relative to the main peaks.

Fig. 7(e) shows the XPS spectra of the Mn 2p core-level for the x = 0.0, 0.5, and 2.0 samples. Deconvolution of the Mn 2p core-level XPS spectra revealed three prominent peaks, where the first two are observed in the range of 640.9–641.4 eV and 642.3–643.0 eV for Mn $2p_{3/2}$ and the third is observed in the range of 652.7–653.5 eV for Mn $2p_{1/2}$. The doublet separation energy (ΔE) for the Mn $2p_{3/2}$ (640.9–641.4 eV)–Mn $2p_{1/2}$ (652.7–653.5) spin–orbit split is observed in the range of 11.8–12.0 eV, which indicates that the Mn ions exist in the +3 oxidation state (Mn^{3+}).[48,52] The other peaks for Mn $2p_{3/2}$ are observed in the range of 642.3–643.0 eV, which are attributed to the Mn^{4+} oxidation state.[53] Based on these characteristic, the Mn cations are present in the mixed valence states of +3 and +4 (*i.e.* Mn^{3+} and Mn^{4+}). Deconvolution of the Mn 2p core-level XPS spectra indicates a considerable increment in the concentration of the Mn^{3+} (73% for x = 0 to 86% for x = 0.5) oxidation state due to Sr^{2+} doping.

The XPS O 1s core-level spectra of the x = 0.0, 0.5, and 2.0 samples are displayed in Fig. 7(f). Two distinct peaks can be observed in the range of 527.9–529.6 eV and 530.1–530.9 eV; (i) the peak centered at ~529 eV is attributed to lattice oxygen (OL), which is associated with the La–O and Fe/Mn–O bonds and (ii) the peak centered at ~531 eV is attributed to surface-adsorbed oxygen from the air, oxygen vacancies (OV) and oxygen species (OH) (*i.e.*, O_2^{2-}, O^{2-}, or O^-), respectively.[48]

3.5 Fourier transform infrared (FTIR) analysis

FTIR spectroscopy provides important information about the bonding between the metal and oxygen ions within the structural lattice. In ABO_3 perovskites, the fundamental IR absorption bands associated with the vibrational frequencies of metal–oxygen bonds typically appear in the range of 400–650 cm^{-1}.[54] Fig. 8 shows the FTIR spectra of the $La_{2-x}Sr_x$-$FeMnO_6$ (where x = 0.0, 0.2, 0.5, 1.0, 1.5, and 2.0) compounds. Two prominent bands can be observed in the FT-IR spectra of all the samples; the first is observed at ~440 cm^{-1} and the second is at ~640 cm^{-1}, which are associated with the Fe–O and Mn–O bond stretching vibrations of the FeO_6 and MnO_6 octahedra, respectively.[55] Further, it was observed that Sr substitution does not introduce any new bands or eliminate existing ones across the entire FTIR spectrum. The position of bands associated with the Fe–O and Mn–O stretching

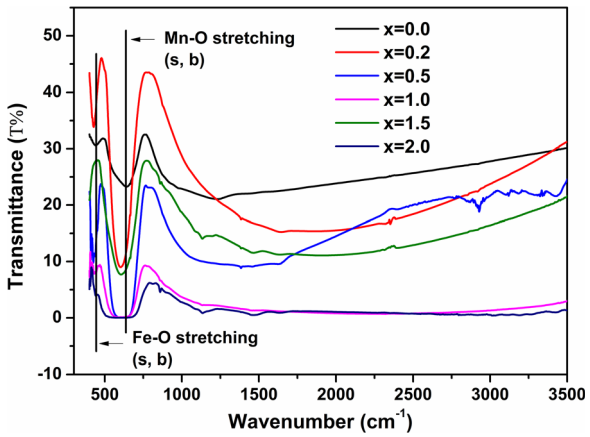

Fig. 8 FTIR spectra of the $La_{2-x}Sr_xFeMnO_6$ (where x = 0.0, 0.2, 0.5, 1.0, 1.5, and 2.0) compounds.

vibrations varies with the Sr concentration. The vibrational band positions of the Fe–O and Mn–O bonds exhibit a noticeable shift toward the higher wavenumber side in the samples with compositions x = 0.5, 1.0, and 2.0, whereas a shift toward the lower wavenumber side is observed for the samples with x = 0.2 and 1.5. Generally, the vibrational frequency of the bond stretching vibrations is determined by the force constant and the reduced mass of the bonded atoms. According to classical mechanics and Hooke's law, the vibrational frequency ($\bar{\upsilon}$) in wavenumber (cm^{-1}) can be expressed as follows:[33,54]

$$\bar{\upsilon} = \frac{1}{2\pi c}\sqrt{\frac{k}{\mu}} \tag{11}$$

where $\bar{\upsilon}$, c, k, and μ are the wavenumber (cm^{-1}), speed of light, force constant of the bond (related to bond strength), respectively, and μ is the reduced mass of the bonded atoms. According to Badger's rule, the force constant (k) can be calculated using the following relation:[33,54]

$$k = \frac{17}{r^3} \tag{12}$$

where r is the bond length between metal–oxygen (M–O) bonds obtained by the crystallographic data in the XRD section (see Table 1). According to eqn (11) and (12), it can be inferred that the bond length (r) is inversely proportional to both the force constant (k) and the vibrational frequency ($\bar{\upsilon}$). The M–O bond length (r) is higher for the x = 0.1, 0.2, and 1.5 samples and lower for x = 0.5, 1.0 and 2.0 compared to the undoped sample (x = 0.0), as given in Table 1. Then the force constant (k) and vibrational frequencies ($\bar{\upsilon}$) of the Fe–O and Mn–O bonds will be lower for x = 0.2 and 1.5, and higher for the x = 0.5, 1.0 and 2.0 samples compared to the undoped La_2FeMnO_6 (x = 0.0) sample.

3.6 DC resistivity analysis

The change in the DC resistivity of the $La_{2-x}Sr_xFeMnO_6$ (where x = 0.0, 0.2, 0.5, 1.5, and 2.0) compounds with temperature (T) is plotted in Fig. 9(a). The semiconducting nature of the synthesized samples can be observed in the temperature range of 150–300 K. In the narrow high temperature region above 250 K, the resistivity data fitted well with the Arrhenius model, as shown in Fig. 9(b). The Arrhenius model is described by the following equation:

$$\rho(T) = \rho_0 \exp\left(\frac{E_a}{k_B T}\right) \tag{13}$$

where ρ_0 is a constant contribution caused by defects, E_a is the energy required for conduction and is called the activation energy, k_B is the Boltzmann constant, and T is temperature. The fitting of the resistivity data at high temperatures indicates that the conduction is primarily governed by long-range percolative transport, where charge carriers move by hopping over energy barriers due to high thermal energy. In this regime, the carriers are effectively excited beyond the mobility edge. The corresponding activation energies are listed in Table 4(a). The resistivity behavior below a temperature of 250 K deviates from that observed at higher temperatures. In this region (low-temperature region), the experimental DC resistivity data are fitted well by the variable range hopping (VRH) model, as shown in Fig. 9(c). The resistivity analysis based on this model indicates that the charge transport occurs *via* phonon-assisted quantum tunneling of the charge carriers to energetically favorable localized states under conditions where thermal energy is significantly lower than the disorder-induced energy (for example, originating from crystal imperfections), which are not necessarily the nearest neighbors. This transport mechanism is commonly referred to as polaron hopping, which predominantly takes place in the vicinity of the Fermi level. According to this model, the temperature dependence of resistivity (ρ) is described by the following expression:

$$\rho(T) = \rho_0 \exp\left(\frac{T_0}{T}\right)^{\frac{1}{4}} \tag{14}$$

where ρ_0 is the pre-exponential factor and T_0 is the characteristic temperature, which are given as follows:

$$\rho_0 = [(3e^2\nu_{ph})/\{8\pi\alpha k_B T/N(E_F)\}^{1/2}]^{-1}$$

and,

$$T_0 = 18\alpha^3/[k_B N(E_F)]$$

where ν_{ph} ($\sim 10^{13}$ s^{-1}), $N(E_F)$, α denote the phonon frequency at the Debye temperature, localized electron states at the Fermi level, and inverse localization length, respectively. At low temperatures, the resistivity behavior of La_2FeMnO_6 is well described by the variable range hopping of small polaron (VRH-SP) conduction in our earlier published paper.[17] The activation energy (E_ρ) for the VRH conduction mechanism can be estimated using the following relation:

$$E_\rho = 0.25 k_B T_0^{1/4} T^{3/4} \tag{15}$$

The estimated activation energy values are given in Table 4(a). The magnitude and trend of the activation energies derived from the linear fitting of resistivity align closely with that reported for other systems exhibiting polaron hopping conduction, including compounds such as $FeTiTaO_6$,[56]

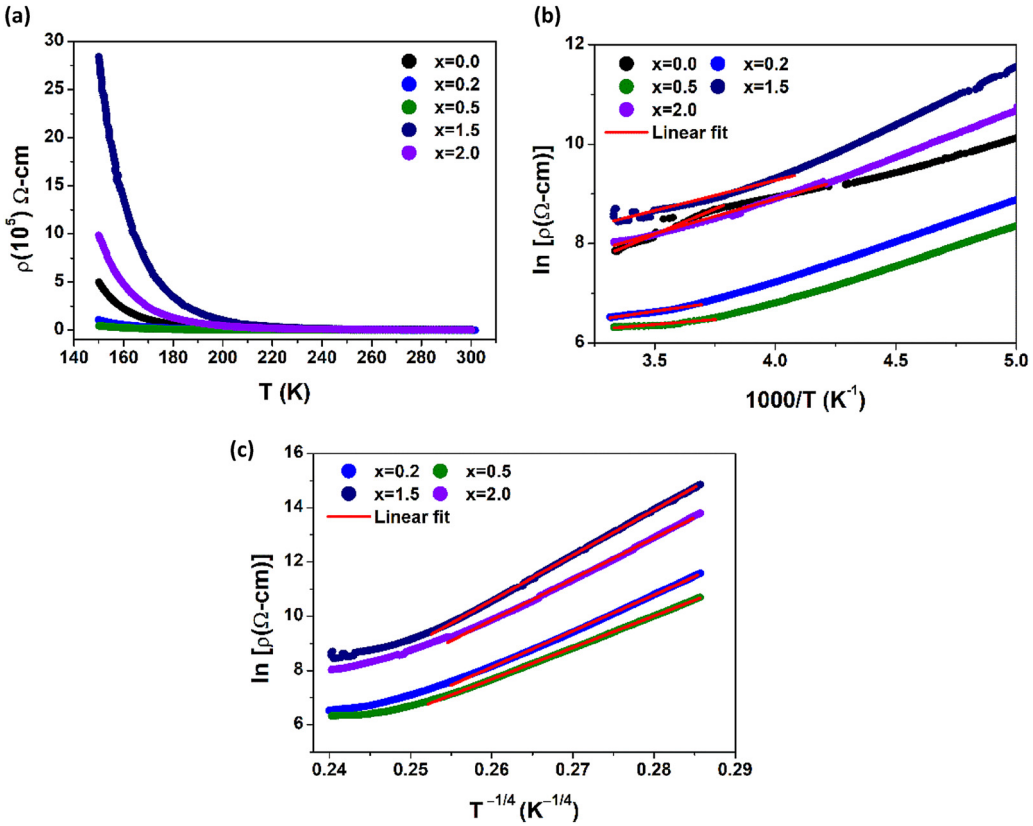

Fig. 9 (a) Temperature dependence of DC resistivity, (b) linear fitting of ln ρ *versus* 1000/T (Arrhenius model), and (c) linear fitting of ln ρ *versus* $T^{-1/4}$ (VRH model) for the $La_{2-x}Sr_xFeMnO_6$ samples.

$Ca_{1-x}Dy_xBaFe_4O_7$,[57] and various manganites.[58–60] A quantitative comparison of the activation energy with some earlier reported systems is given in Table 4(b). The hopping range (R) can be approximated utilizing the following expression:

$$R \approx 0.2686\xi\left(\frac{T_0}{T}\right)^{\frac{1}{4}} \quad (16)$$

where ξ denotes the decay length of the polaronic wave function. In oxide materials, electron injection typically arises from the formation of random oxygen vacancies, which subsequently undergo ionization to contribute free electrons.[61,62] Furthermore, the material under investigation exhibits an irregular arrangement of $Fe^{3+/4+}$ and $Mn^{3+/4+}$ ions, potentially indicating improper charge ordering. At low temperatures, electrons are expected to remain localized within the potential wells formed by the Fe and Mn cations. The average distance of Fe–Mn, Fe–Fe, and Mn–Mn separation can serve as a calculation of the decay length ξ in the corresponding equation. The averaged values are used to estimate ξ, which in turn allows the calculation of the hopping range R, as given in Table 4(a). The resulting R values suggest that the polaron transport occurs *via* a short-range variable-range hopping (VRH) mechanism, consistent with findings reported in previous studies.[57,63] At this stage, it is important to acknowledge that the DC resistivity measurement reflects contributions from both grain boundaries and the intrinsic properties of individual grains. However, in bulk samples such as those studied here, the resulting parameters and their functional behavior remain largely consistent with those expected from an ideal sample. The intrinsic grain response associated with DC resistivity can be extracted from AC measurements.

3.7 Dielectric analysis

Fig. 10(a) shows the frequency-dependent variation in the real dielectric constant (ε') in the frequency range of 700 Hz to 2 MHz for the $La_{2-x}Sr_xFeMnO_6$ (where x = 0.0, 0.1, 0.2, 0.5, 1.0, 1.5, and 2.0) compounds at RT. The real part of the dielectric constant (ε') exhibits higher values at lower frequencies, and it decreases sharply with an increase in frequency up to a certain value; beyond this, it reaches a steady state at higher frequencies. The higher value of ε' at low frequencies is primarily attributed to interfacial space charge polarization at the interfaces between the conducting grains and insulating grain boundaries.[64,65] At higher frequencies, the reduction in ε' is due to the inability of charge carriers to align with the rapidly alternating electric field,[66] causing electronic and/or ionic polarization to become dominant.[34] Further, for the x = 0.1, 0.2 and 1.0 samples, the value of ε' becomes negative *via* crossing zero at a specific frequency point. Other cermets have been reported to exhibit similar phenomena at higher frequency.[67–69] Generally, negative permittivity is caused by the plasma oscillations of free or delocalized electrons and

Table 4 (a) Parameters derived from the DC resistivity analysis based on the Arrhenius and variable range hopping (VRH) models. (b) Comparison of the activation energy (E_ρ) derived from the VRH model with some earlier reported manganites

(a)	Arrhenius model		VRH model				
Sr concentration (x)	E_a (meV)	T range (K)	$T_0^{1/4}$ ($K^{1/4}$)	E_ρ (meV)	ξ (Å)	R (Å)	T range (K)
x = 0.0	176	264–300	—	—		—	—
x = 0.2	060	271–300	133.40(±0.1)	124–174	3.9096	40–35	151–237
x = 0.5	035	266–300	116.77(±0.1)	108–157	3.8908	35–30	150–248
x = 1.5	105	245–300	166.98(±0.1)	155–223	5.5176	70–62	152–245
x = 2.0	120	237–300	151.26(±0.3)	141–197	3.8550	44–39	152–237

(b)			
Compounds	E_ρ (meV)	T range (K)	Ref.
$FeTiTaO_6$	140–260	123–293 K	56
$Ca_{1-x}Dy_xBaFe_4O_7$			57
x = 0.00	128–175	145–220	
x = 0.01	183–228	159–213	
x = 0.03	198–259	140–200	
x = 0.05	90–125	127–197	
$Pr_{0.6}Sr_{0.4}Mn_{0.6}Ti_{0.4}O_{3\pm\delta}$	113–303	130–275	58
$La_{0.9}Sr_{0.1}MnO_3$	71–105	170–280	59
$La_{0.8}Na_{0.2}MnO_3$	83–142	220–460	60
$Ni_{0.5}Zn_{0.5}Fe_2O_4$	143–223	130–235	63 [Fig. 3]
$La_{2-x}Sr_xFeMnO_6$			This paper
x = 0.2	124–174	151–237	
x = 0.5	108–157	150–248	
x = 1.5	155–223	152–245	
x = 2.0	141–197	152–237	

dielectric resonance phenomenon within a material.[40,68–70] This phenomenon is commonly observed in metals, semiconductors and metamaterials, or inductive effects from percolating conductive networks. Under the influence of an external electric field, both free electrons and localized charges contribute to the dielectric response. In contrast, localized charges tend to align with the applied electric field through polarization and free electrons undergo collective oscillations (known as plasma oscillations) along the direction of the field.[40,68] The dielectric resonance of a dielectric usually occurs under an applied electric field when the frequency of the applied electric field is the same as the natural vibrational frequency of various micro entities in the samples, which may be atoms, valence electrons, and an inner-electrons. This resonance usually occurs at higher frequencies. With an increase in the applied frequency, the permittivity of the material changes from positive to negative at a particular frequency. At high frequencies, the speed of polarization switching lags far behind the applied electric field. As a result, the electric field increases toward the positive direction, leading to polarization in the negative direction due to the phase angle difference between the polarization vector and applied electric field.[68,69] In this case, negative permittivity occurs in a narrow frequency region just above the resonance frequency (ω_0), before becoming positive again at higher frequencies. This is an obvious phenomenon of dielectric resonance, which can be explained by the Lorentz model,[67,68] as follows:

$$\varepsilon'(\omega) = 1 + \frac{K\omega_0^2(\omega_0^2 - \omega^2)}{(\omega_0^2 - \omega^2)^2 + \Gamma_L^2\omega^2} \quad (17)$$

where Γ_L is the damping factor of the Lorentz resonance, ω_0 is the Lorentz resonance frequency, and K is the polarizability under a DC electric field. When the frequency (ω) under the applied electric field is just above the resonance frequency (ω_0) of the material, negative permittivity occurs.

Fig. 10(b) shows the frequency-dependent variation in dielectric loss tangent ($\tan\delta$) for the $La_{2-x}Sr_xFeMnO_6$ samples in the frequency range of 700 Hz to 2 MHz. This behavior is primarily attributed to interfacial space charge polarization effects.[20] Additionally, it is observed that the loss tangent value increases for Sr substitution. In contrast, for the x = 0.1 and 1.0 samples, the loss tangent value decreases compared to the undoped sample. The variation in ε' and $\tan\delta$ with Sr concentration can be governed by several defects such as more modest grain size, distortion/stress, strain, and oxygen vacancy created by Sr substitution in the $La_{2-x}Sr_xFeMnO_6$ semiconducting material.[20,34] All these defects can lead to variations in the conductivity of the material, as further evidenced by AC conductivity measurements. All the synthesized samples exhibit frequency-dependent dispersion and relaxation in their dielectric constants. Among them, the sample with the composition x = 0.1 demonstrates a comparatively higher dielectric constant across the measured frequency range. Particularly, the dielectric loss tangent ($\tan\delta$) for the x = 0.1 sample remains lower than that of the other compositions in the entire frequency range, except for x = 1.0. The best combination of high dielectric constant and low dielectric loss for the x = 1.0 sample suggests that it possesses superior energy storage capability compared to the other synthesized samples. The detailed frequency-dependent dielectric parameters are summarized in

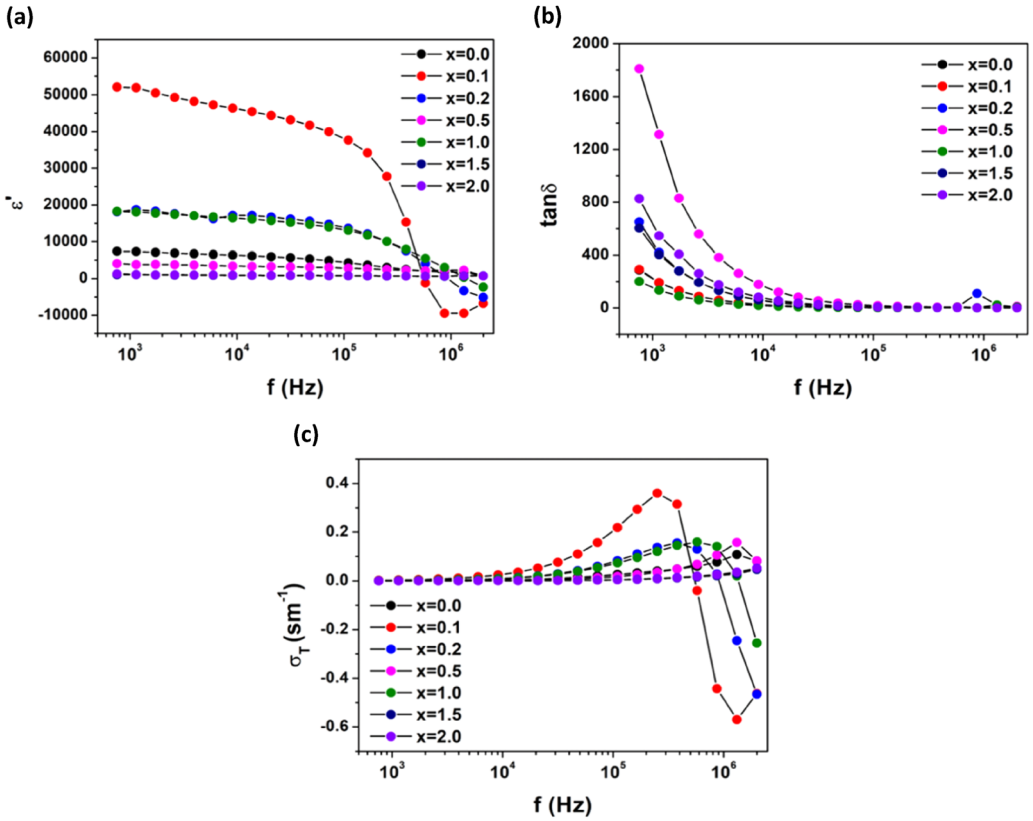

Fig. 10 Frequency dependence of (a) dielectric constant, (b) dielectric loss tangent (tan δ), and (c) AC conductivity of the $La_{2-x}Sr_xFeMnO_6$ samples at room temperature.

Table 5(a). This finding demonstrates that the dielectric constant and dielectric loss tangent of La_2FeMnO_6 are greatly affected by Sr substitution. In our previous study,[34] we have reported the highest dielectric constant of $\sim 1.52 \times 10^4$ at 4 kHz near room temperature (RT) for the $La_{2-x}Ca_xFeMnO_6$ system with the composition x = 0.1 (*viz*, $La_{1.9}Ca_{0.1}FeMnO_6$), and presented a brief comparison with some earlier reported high dielectric materials. In this study, the dielectric constant was determined to be $\sim 4.8 \times 10^4$ at 4 kHz near RT for the $La_{2-x}Sr_xFeMnO_6$ system with the x = 0.1 composition, which can make it more interesting for application in advanced technologies as a high dielectric material compared to earlier reported dielectric materials (Table 5 in ref. 34). Colossal/giant dielectric ($\varepsilon' \geq 10^3$) materials are not widely used as commercial dielectric materials in industrial applications due to their high energy loss but they are an active area of research for potential future applications. However, the highest obtained dielectric constant value for the x = 0.1 (*viz*, $La_{1.9}Sr_{0.1}FeMnO_6$) sample is compared with some existing commercial as well as non-commercial dielectric materials, as listed in Table 5(b).

The AC conductivity (σ_{ac}) of the $La_{2-x}Sr_xFeMnO_6$ material was determined using the following expression:

$$\sigma_{ac} = 2\pi f \varepsilon' \varepsilon_0 \tan\delta \quad (18)$$

where f denotes the applied frequency, ε_0 is the permittivity of free space, ε' refers to the real component of the dielectric constant, and tan δ indicates the dielectric loss factor. The change in AC conductivity with Sr substitution [Fig. 10(c)] may be attributed to the development of modest grain and enhanced grain boundary effects related to higher grain boundary density and multiple polarization phenomena.[87] The AC conductivity is also influenced by the presence of oxygen vacancies within the samples. Further, an increase in conductivity is observed with an increase in frequency up to a certain value (threshold), which is attributed to the hopping conduction mechanism in the materials. Beyond this frequency, σ_{ac} starts to decrease and becomes negative at a MHz frequency, which can be explained by the following expression:[88]

$$\sigma_{ac} = n_0 e(M_i - M_e)E \quad (19)$$

where n_0 is the number density of electrons, e is the charge of electrons, M_e denotes the mobility of electrons, M_i denotes the mobility of ions, and E is the strength of the applied electric field. Given that electrons are significantly lighter than ions, the mobility of electrons is higher than that of ions, which is more significant in the higher frequency regime. According to eqn (19), above the plasma resonance frequency (ω_0), the conductivity (σ_{ac}) starts to decrease and after a certain value (above plasma resonance frequency), it becomes negative. This decrement in σ_{ac} at higher frequencies can be attributed to the skin effect,[40] a phenomenon wherein an alternating current tends to flow predominantly along the surface of a conductor at

Table 5 (a) Real dielectric constant (ε'), tangent dielectric loss (tan δ), and AC conductivity (σ_{ac}) for the $La_{2-x}Sr_xFeMnO_6$ (where x = 0.0, 0.1, 0.2, 0.5, 1.5, and 2.0) compounds near room temperature at 757 Hz and 1 MHz. (b) Quantitative comparison of the dielectric constant (ε') of the $La_{1.9}Sr_{0.1}FeMnO_6$ (x = 0.1) sample with those of some earlier reported dielectric materials at room temperature (RT)

(a)	Frequency at 757 Hz			Frequency at 1 MHz		
Concentration (x)	ε' ($\times 10^4$)	Tan δ ($\times 10^2$)	$\sigma_{ac} \times 10^{-4}$ (S m^{-1})	ε' ($\times 10^4$)	Tan δ ($\times 10^2$)	$\sigma_{ac} \times 10^{-4}$ (S m^{-1})
0.0	0.74	2.85	3.11	0.17	0.017	1072
0.1	5.21	2.91	21.9	−0.94	0.014	−5700
0.2	1.80	6.50	7.61	−0.33	0.215	−2455
0.5	0.41	18.09	1.71	0.23	0.026	1567
1.0	1.82	2.01	7.67	0.30	0.034	1407
1.5	0.10	6.03	0.43	0.07	0.006	281
2.0	0.13	8.26	0.54	0.07	0.008	350

(b)

S. no.	Compounds	Dielectric constant (ε') at RT	Dielectric loss (tan δ)	Synthesis method	Ref.
1	$(1-x)K_{0.5}Na_{0.5}NbO_{3-x}Bi$ $(Li_{0.5}Ta_{0.5})O_3$ (x = 0, 0.05, 0.10, 0.15, 0.20)	∼850–1200 @ 1 kHz	0.01–0.9	Solid-state reaction	71
2	$Sr_{1-x}Ca_xTiO_3$ (x = 0, 0.02, 0.04 and 0.08)	∼275–335 @ 1 kHz	2×10^{-3}	Solid state reaction	72
3	$(Ba_{0.7}Sr_{0.3})_{1-x}Nd_xTi_{1-y}Mn_yO_3$ (x = 0; y = 0) − (x = 0.005; y = 0)	∼(1.9–2.0) $\times 10^3$ @ 1 kHz	(2.18–2.66) $\times 10^{-2}$	Solid-state reaction	73
4	Al_2O_3	∼2.8 $\times 10^4$ @ 1 kHz	0.12	Colloidal processing	74
5	$Ti_{1-x}Fe_xO_2$ (x = 0, 0.02, and 0.05)	∼105, 84, and 76 @ 1 kHz	—	Sol–gel	75
6	$La_{0.67}Li_xTi_{1-x}Al_xO_3$ (where x = 0.05, 0.2, 0.3)	∼10^4–10^5 @ 1 kHz	1.4–1.8	Sol–gel Pechini method	76
7	Steatite	6.0 @ 1 Hz 5.7–6.5 @ 1 MHz	(1.4–22) $\times 10^{-3}$ (1–6) $\times 10^{-3}$	Commercial	77
8	Al_2O_3	8.0–9.0 @ 1 Hz 7.8–11 @ 1 MHz	(3.1–11) $\times 10^{-4}$ (4.9–13) $\times 10^{-4}$	Commercial	78
9	ZrO_2	28	—	Commercial	79
10	$ZrSiO_4$	8.8	—	Commercial	80
11	Porcelain	5–10 @ 1 Hz 6.5 @ 1 MHz	(4.3–28) $\times 10^{-3}$ (4.3–130) $\times 10^{-4}$	Commercial	81
12	$BaTiO_3$	1.2 $\times 10^3$ @ 1 kHz	3.78 $\times 10^{-3}$	Bell Telephone Laboratories	82
13	$LaBaFeTiO_6$ $EuBaFeTiO_6$	∼400 @ 10 kHz ∼75 @ 10 kHz	∼1.0 ∼0.5	Solid-state reaction	83
14	$La_2FeReO_{6+\delta}$	∼300 @ 1 kHz	∼2.5	Solid-state reaction	84
15	$CaBiFeMnO_6$	∼4 $\times 10^4$ @ 100 Hz	∼9.01	Solid-state reaction	22
16	$Co_{0.65}Zn_{0.35}Fe_2O_4$	∼7 $\times 10^3$ @ 1 kHz	∼1	Solid-state reaction	19
17	$Co_{1-x}Ni_xFe_2O_4$ (x = 0.0, 0.25, 0.5, 0.75, 1.0)	∼100–200 @ 1 kHz	∼2	Combustion	20
18	$La_{1.9}Ca_{0.1}FeMnO_6$	∼1.4 $\times 10^4$ @ 1 kHz	∼122	Solid-state reaction	34
19	$Nd_{2-x}Sr_xNiMnO_6$ (x = 0.0, 0.1, 0.3)	∼(4.5, 7.5, 8.2) $\times 10^3$ @ 1 kHz	∼120, 30, 158	Solid-state reaction	39
20	$La_2Co_{1-x}Ni_xMnO_6$ (x = 0, 0.1, 0.5)	∼(4.6, 5.8, 5.8) $\times 10^3$ @ 1 kHz	∼10, 32, 85	Sol–gel	85
21	Nd_2CoIrO_6	∼5800 @ 1 kHz	—	Solid-state reaction	86
22	$La_{1.9}Sr_{0.1}FeMnO_6$	∼5.1 $\times 10^4$ @ 1 kHz −0.94 $\times 10^4$ @ 1 MHz	∼193 ∼1.4	Solid-state reaction	This work

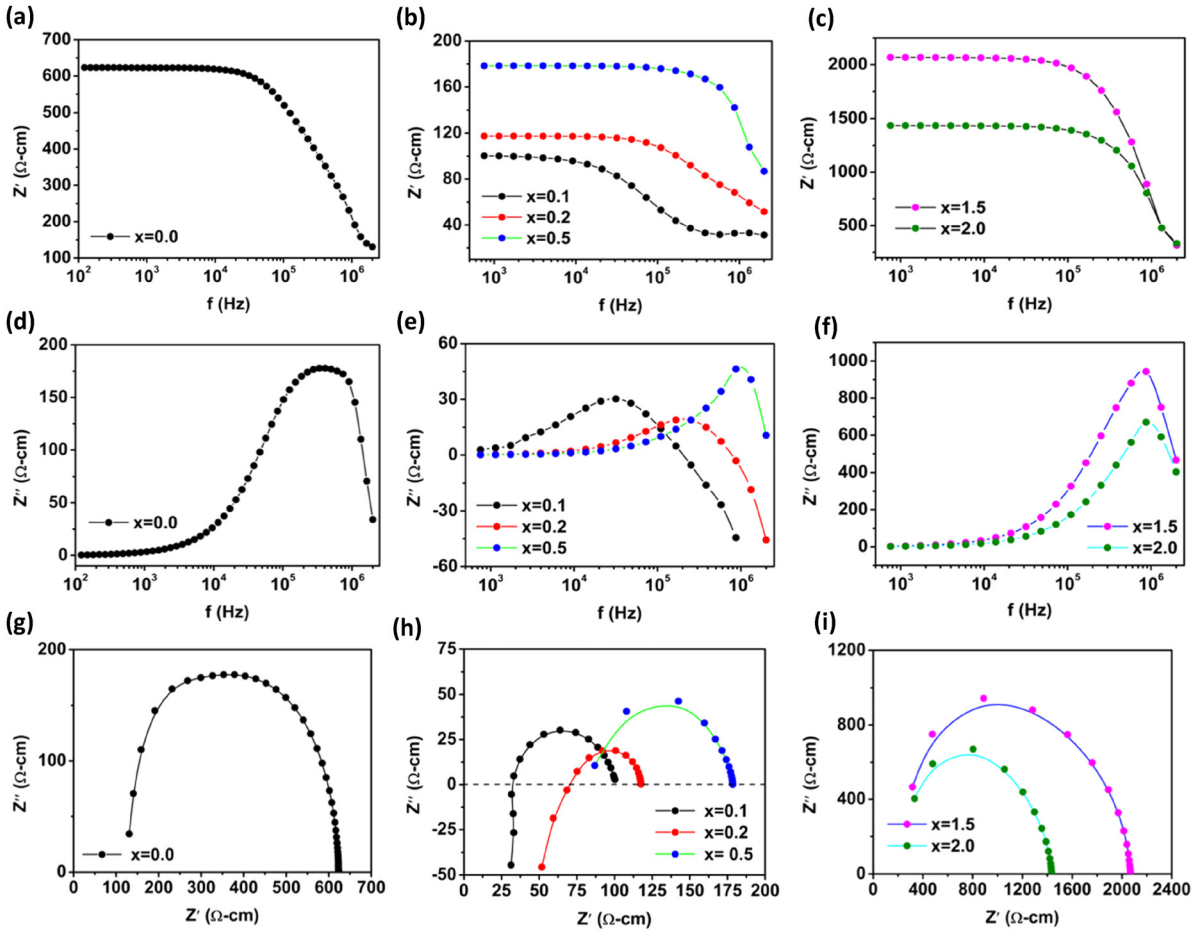

Fig. 11 Frequency dependence of the real part of impedance (Z') (a)–(c), imaginary part of impedance (Z'') (d)–(f), and Nyquist plots (Z'' *vs.* Z') (g)–(i) for the $La_{2-x}Sr_xFeMnO_6$ samples (where, x = 0.0, 0.1, 0.2, 0.5, 1.5, and 2.0) at RT.

elevated frequencies. As the frequency increases, this effect leads to an increase in effective resistance, thereby diminishing the overall conductivity. This phenomenon occurs due to the self-induced magnetic field generated by the alternating current, which causes the electrons to become concentrated near the surface of the conductor. As a result, at higher frequencies, the current is confined to a thinner surface layer, effectively reducing the cross-sectional area available for conduction. This leads to an increase in resistance and a corresponding decrease in conductivity. The depth to which the current penetrates the surface is known as the "skin depth." This parameter is inversely proportional to the square root of both the frequency and conductivity of the material.

Fig. 11(a)–(c) display the variation in the real part of impedance (Z') of all the synthesized samples with applied frequency in the range of 700 Hz to 2 MHz. The value of Z' remains constant up to a threshold frequency, after which it starts to decrease with an increase in frequency and tends to merge at higher frequencies. This behavior can be explained by the loss of space charge polarization and decreased in the grain boundary effects in the material.[89] This pattern suggests an increment in the electrical conduction of the materials and it corroborates the earlier obtained AC conductivity results. Fig. 11(d)–(f) display the variation in imaginary part of impedance as a function of frequency (100 Hz to 2 MHz). A single relaxation peak can be observed for all the samples, confirming the existence of relaxation phenomena. The frequency f at which Z'' attains its peak is known as the relaxation frequency (f_r). The relaxation time τ can be calculated using the relation $\tau = 1/2\pi f_r$.[34] A single relaxation peak clearly indicates the contributions of the grain boundary effect. In all the synthesized bulk samples, the electrical response of the grain boundary can be considered an electrical circuit consisting of a parallel combination of resistance, R_{gb}, and capacitance, C_{gb}. The resistivity associated with the grain boundary (ρ_{gb}) can be estimated using the relaxation peak intensity. The peak intensity is equal to half of the grain boundary resistivity ($\rho_{gb}/2$).[86] The grain boundary capacitance (C_{gb}) can be estimated using the relaxation peak frequency (f_{rgb}) based on the relation $C_{gb} = 1/(2\pi f_{rgb}\rho_{gb})$. The corresponding relaxation time (τ_{gb}) can be calculated using the expressions $\tau_{gb} = 1/2\pi f_{rgb} = \rho_{gb}C_{gb}$. The calculated values are given in Table 6.

Fig. 11(g)–(i) display a depressed single semicircular arc (impedance Nyquist plot) with its center positioned below the real axis for all the synthesized samples. The semicircular arcs in the Nyquist plot indicate that the conductivity arises from

Table 6 Parameters of $La_{2-x}Sr_xFeMnO_6$ (where x = 0.0, 0.1, 0.2, 0.5, 1.5, and 2.0) obtained from impedance analysis

Sr concentration (x)	f_{rgb} (Hz)	ρ_{gb} (Ω cm)	C_{gb} (pF cm^{-1})	τ_{gb} (μs)
0.0	373 255	356	1179	0.42
0.1	30 637	62	83 871	5.20
0.2	206 714	38	20 263	0.77
0.5	1 005 337	95	1684	0.16
1.5	803 433	1903	105	0.20
2.0	906 764	1342	126	0.17

contributions by either the grains or the grain boundaries. The presence of a single semicircle highlights the significant influence of the grain boundary effect. The depressed semicircular arcs indicate the non-Debye type relaxation in all the measured samples.

3.8 Magnetic analysis

The field-dependent magnetic properties (M–H loop) of the $La_{2-x}Sr_xFeMnO_6$ materials (where x = 0.0, 0.1, 0.2, 0.5, 1.0, 1.5, and 2.0) were recorded in the range of −20 kOe to +20 kOe at RT. The diversity in magnetic behavior of all the synthesized materials is displayed in Fig. 12. The observed M–H curve is not linear, while it shows a small hysteresis loop at room temperature, which denotes that the antiferromagnetic (AFM) nature no longer exists in the $La_{2-x}Sr_xFeMnO_6$ (x = 0.0, 0.1, 0.2, 0.5, 1.0 and 1.5) compounds. They started to show weak ferromagnetic (FM) behavior at a low magnetic field strength. In contrast, the sample with the x = 2.0 composition exhibits linear field-dependent magnetization, which is characteristic of paramagnetic (PM) materials. In all the samples, the magnetization increases with an increase in the strength of the applied magnetic field but does not reach saturation, which is the signature of complex magnetic behavior of AFM and FM/ferrimagnetic (FIM).[17] The XPS analysis reveals that the Fe and Mn cations exhibit +3 and +4 mixed valence states in all the synthesized materials. Therefore, there are several possible magnetic interactions (FM, FIM and AFM) between the Fe and Mn cations with an oxygen mediator.[34] The origin of the non-linear behavior of the M–H loop with weak ferromagnetism was explained well in our earlier published papers.[17,34] The corresponding values of maximum magnetization (M_m), coercive field (H_c), remnant magnetization (M_r), and remanence ratio (M_r/M_m) for all the prepared samples were obtained from their hysteresis loop, which are listed in Table 7. The magnetic moment of all the synthesized samples was estimated from their corresponding magnetization data using the following relation:[33]

$$\eta_B = \frac{\text{Molecular weight}}{5585} \times M_m \quad (20)$$

where η_B represents the magnetic moment and M_m denotes the maximum magnetization. The estimated value of magnetic moment is listed in Table 7.

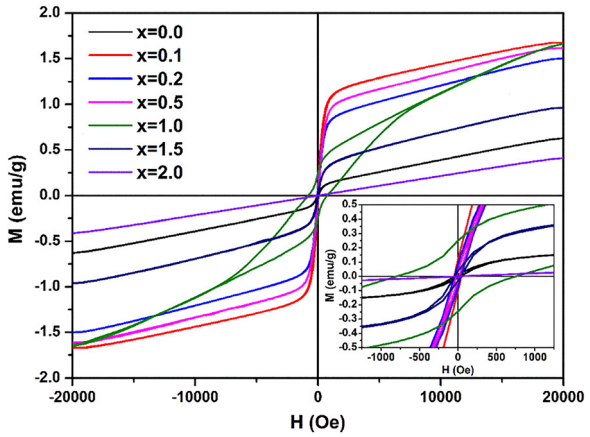

Fig. 12 Magnetic hysteresis (M vs. H) loop for the $La_{2-x}Sr_xFeMnO_6$ (where x = 0, 0.1, 0.2, 0.5, 1.0, 1.5, and 2.0) materials at room temperature.

3.9 I–V characteristics

The current–voltage (I–V) measurement is an important technique for evaluating the performance of electronic devices. It provides essential insight into their functionality. Noticing the importance of this measurement, we recorded the I–V curves of the $La_{2-x}Sr_xFeMnO_6$ materials at RT. All the synthesized materials exhibit a colossal/giant dielectric constant, as discussed in the previous section. Therefore, it is essential to examine their I–V characteristics for emerging potential applications in electronic devices. Fig. 13(a) shows the variation in current with applied electric field at RT for all the synthesized samples. Here, it can be observed that the conduction current exhibits a nonlinear increase with the applied electric field strength, indicating the semiconducting diode-type nature of all the samples. Hence, they can be used as a rectifier in appropriate electronic devices as a diode. Fig. 13(b) illustrates the relationship between the leakage current density (J) and the applied electric field (E) at RT for all the synthesized compounds. As the

Table 7 Maximum magnetization (M_m), coercive field (H_c), remnant magnetization (M_r), remanence ratio (M_r/M_m), and magnetic moment (η_B) values for $La_{2-x}Sr_xFeMnO_6$ (where x = 0.0, 0.1, 0.2, 0.5, 1.0, 1.5, and 2.0) at room temperature

Concentration (x)	M_m (emu g^{-1})	M_r (emu g^{-1})	H_c (Oe)	M_r/M_m	η_B (BM)
x = 0.0	0.62	0.01	035	0.016	0.053
x = 0.1	1.67	0.10	045	0.059	0.143
x = 0.2	1.50	0.08	042	0.053	0.127
x = 0.5	1.62	0.03	018	0.018	0.133
x = 1.0	1.65	0.25	775	0.151	0.128
x = 1.5	0.96	0.04	040	0.001	0.070
x = 2.0	0.41	0.00	000	0.000	0.028

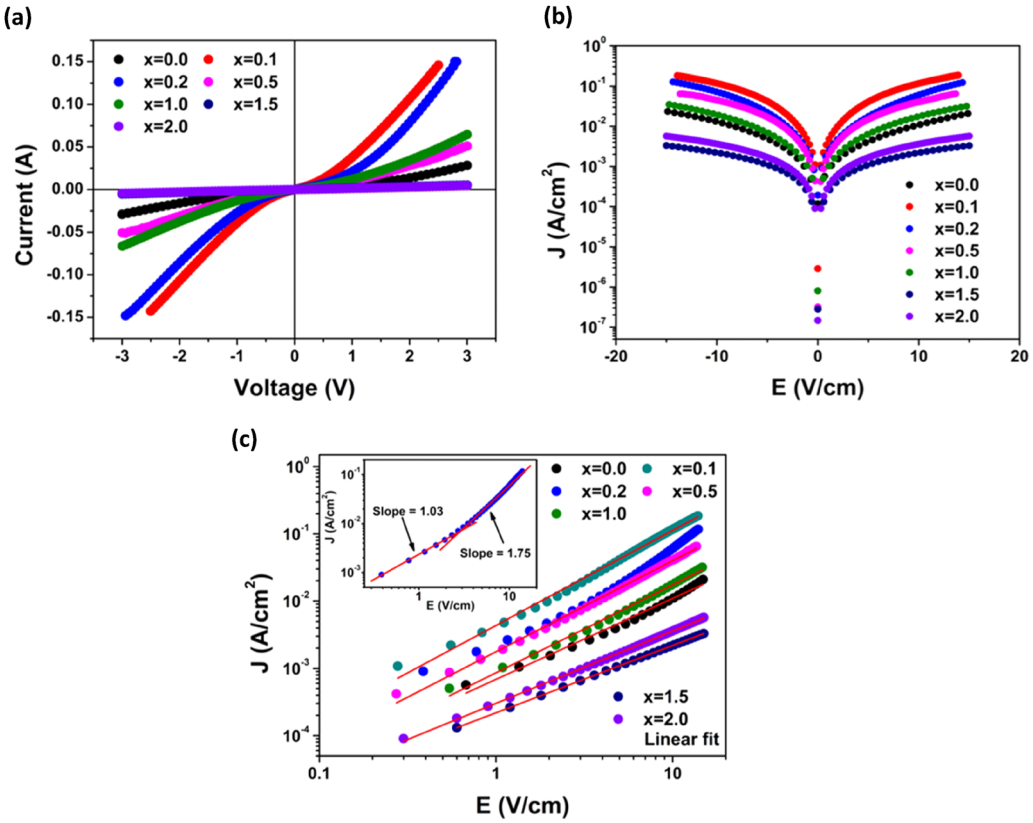

Fig. 13 Electric field-dependent current (a) and leakage current density (J) (b); linear fitting of log(J) *vs.* log(E) curves (c) for the $La_{2-x}Sr_xFeMnO_6$ samples at RT and inset of (c) shows two different slopes in two different regions for x = 0.2 sample.

Table 8 Lowest leakage current density of some compounds at room temperature

Compounds	Lowest J (A cm^{-2})@RT	Ref.
$(1-x)Bi_{1+y}FeO_{3-x}BaTiO_3$		92
$0.25 \leq x \leq 0.40$; $y = 0.00$	$\sim 10^{-7}$–10^{-8}	
$-0.02 \leq y \leq 0.04$; $x = 0.30$	$\sim 10^{-7}$–10^{-9}	
$(1-x)Bi_{0.48}La_{0.02}Na_{0.48}Li_{0.02}Ti_{0.98}Zr_{0.02}O_{3-x}Na_{0.73}Bi_{0.09}NbO_3$ (x = 0–0.14)	$\sim 10^{-4}$–10^{-5}	93
La_2FeMnO_6	$\sim 10^{-4}$	17
$(K_{0.44},Na_{0.52},Li_{0.04})$ $(Nb_{0.84},Ta_{0.1},Sb_{0.06}O_3)$ KNN-LT-LS	$\sim 10^{-8}$	90
$CaBiFeMnO_6$	$\sim 10^{-7}$	22
Nd_2NiTiO_6	$\sim 10^{-7}$	94
$La_{2-x}Ca_xFeMnO_6$ (x = 0.0, 0.1, 0.2, and 0.5)	$\sim 10^{-4}$–10^{-5}	34
$La_{2-x}Sr_xFeMnO_6$ (x = 0.0, 0.1, 0.2, 0.5, 1.0, 1.5, and 2.0)	$\sim 10^{-4}$–10^{-7}	This work

electric field increases, the leakage current density also increases. The increase in leakage current density could be attributed to some factors such as the influence of the potential barrier, structural distortions or defects, and the presence of polarized charges under an applied external field.[90,91] The trend of change in leakage current density with an increase in applied electric field strength is similar to some earlier reports.[17,22,34,90,92–94] All the synthesized materials might be suitable for application in electronic devices because of their low leakage current density ($\sim 10^{-1}$–10^{-7} A cm^{-2}) observed in the electric field range of −15 to +15 V cm^{-2}. It has also been observed that the leakage current density primarily increases for x = 0.1, and then it starts to decrease with an increase in Sr concentration, giving the lowest leakage current density ($\sim 10^{-7}$ A cm^{-2}) for x = 2.0. Thus, it becomes more promising for application in electronic devices than the others. A quantitative comparison of the leakage current density values with some earlier reported compounds is given in Table 8.

The substitution of Sr at the La site leads to stress and structural distortion because of the difference in their ionic sizes (as discussed earlier in the XRD section), resulting in the creation of Schottky defects. Additionally, the presence of mixed valence states of Mn and Fe (*i.e.*, Mn^{3+}, Mn^{4+}, Fe^{3+}, and Fe^{4+}) contributes to the formation of oxygen vacancies to preserve charge neutrality, which is confirmed by the XPS analysis. The applied external electric field can activate these

multiple valence states, generating free charge carriers, which contribute to the resulting leakage current. There are several potential mechanisms that can explain the limitations of the leakage current in insulating and/or semiconducting materials. These mechanisms are generally categorized into two groups, as follows: (I) interface-limited conduction mechanisms and (II) bulk limited conduction mechanisms. A linear increment in leakage current density with the applied electric field indicates Ohmic conduction behavior. To confirm the conduction mechanism in the $La_{2-x}Sr_xFeMnO_6$ compound, its leakage current density (J) was plotted against the applied electric field (E) on a logarithmic scale [log(J) *vs.* log(E)], as illustrated in Fig. 13(c). All these plots exhibit a good linear fit with different slopes. These slopes are close to 1 ($S \approx 1$), indicating linear Ohmic conduction in all the samples. In the case of $x = 0.2$, the linear log(J) *vs.* log(E) plot was fitted with two distinct slopes, as shown in the inset of Fig. 13(c). The slope (S) is close to 1 in the lower electric field region. Alternatively, in the higher electric field region, the slope is approximately 1.75, indicating space-charge-limited conduction (SCLC).[95] Both Ohmic and SCLC conduction are associated with the bulk limited conduction mechanism. The leakage current density associated with Ohmic conduction can be expressed by the following equation:

$$J = q\mu \mathrm{Ne}E \tag{21}$$

where Ne represents the density of thermally activated electrons, μ is the mobility of charge carriers, and q is the charge of an electron. Further, in the higher electric field region, space-charge-limited conduction (SCLC) occurs due to the accumulation of space charge near the electrodes. The accumulation of space charge occurs when charge carriers are injected from the electrode into the material at a rate exceeding their transport. The current density for the SCLC mechanism can be expressed as follows:

$$J_{\mathrm{SCLC}} = \frac{9\mu\varepsilon_r\varepsilon_0\theta E^2}{8d} \tag{22}$$

where μ represents the carrier mobility, d represents the thickness of the pellet, and θ is the fraction of injected charge carriers ($\theta = 1$ in trap-free limit). Hence, the change in slope from 1.03 to 1.75 (for $x = 0.2$) indicates a transition in conduction mechanism from Ohmic to SCLC.

4. Conclusion

Polycrystalline $La_{2-x}Sr_xFeMnO_6$ (where $x = 0.0$, 0.1, 0.2, 0.5, 1.0, 1.5, and 2.0) samples were successfully prepared *via* the solid-state reaction method. The Rietveld refinement of their XRD data shows the re-entrant structural phase transition (cubic–rhombohedral–cubic) of the disordered $La_{2-x}Sr_xFeMnO_6$ materials with Sr-doping. The SEM study shows anisotropic their thermal expansion during grain formation, which leads to the development of micro porosity. Two prominent phonon modes (A_{1g} and B_{1g}) are observed in the Raman spectra of all the synthesized samples, which are associated with the anti-stretching and/or bending and the stretching (''breathing'') vibrations of (Fe/Mn)O_6 octahedra, respectively. The XPS study reveals the presence of mixed valence states of Mn and Fe (*i.e.*, Mn^{3+}, Fe^{3+}, Mn^{4+}, and Fe^{4+}) ions in all samples, which contribute to the formation of oxygen vacancies. The semiconducting nature of all the synthesized samples was determined by their temperature-dependent DC resistivity. The charge conduction in all the synthesized samples has been explained by the long-range electron hoping conduction mechanism in the high temperature region and short-range polaron hopping conduction mechanism in the low-temperature region. The dispersion behavior of the dielectric constant with frequency at RT is the contribution of Maxwell–Wagner interfacial polarization. The highest dielectric constant ($\varepsilon' \sim 5.21 \times 10^4$) was observed for 5% Sr doping at 700 Hz near RT. The Nyquist complex impedance plot indicates non-Debye-type relaxation in all samples. All the synthesized samples exhibit weak ferromagnetism, in contrast to $x = 2.0$, which is paramagnet in nature. The highest ferromagnetic strength ($H_c = 775$ Oe) was observed for 50 Sr doping (*i.e.*, $x = 1.0$). The sample with the composition $x = 2.0$ exhibits the lowest leakage current density ($\sim 10^{-7}$ A cm^{-2}), which makes it the most promising for electronic device applications.

Author contributions

Baniya R. Meena: conceptualization, methodology, investigation, data curation, software, visualization, validation, results interpretation, formal analysis, writing – original draft, writing – review and editing. Anup K. Ghosh: conceptualization, methodology, project administration, validation, supervision, funding acquisition, formal analysis, writing – review and editing.

Conflicts of interest

There are no conflicts to declare.

Data availability

The authors declare that all the data used in this work will be available if and when required.

Acknowledgements

Anup K. Ghosh is thankful to DST-SERB, India (Grant No. CRG/2019/000896) and IoE (Scheme No. 6031) for the financial support. Baniya R. Meena is thankful to the CSIR, India, (File No. 09/013(0957)/2020-EMR-I) and IoE (Scheme: Credit-Research Incentive to Research Scholar, CPB no. 0300) for providing the financial support. Authors acknowledge the Central Research Facility, Department of Physics, BHU, for providing the instruments and support for various characterizations and measurements. Central Discovery Center (CDC), BHU, is also acknowledged by the authors for providing the Raman and XPS facilities.

References

1 M. Jabłońska and R. Palkovits, Perovskite-based catalysts for the control of nitrogen oxide emissions from diesel engines, *Catal. Sci. Technol.*, 2019, **9**, 2057–2077, DOI: 10.1039/C8CY02458H.

2 E. A. R. Assirey, Perovskite synthesis, properties and their related biochemical and industrial application, *Saudi Pharm. J.*, 2019, **27**, 817–829, DOI: 10.1016/j.jsps.2019.05.003.

3 H. Zhu, P. Zhang and S. Dai, Recent advances of lanthanum-based perovskite oxides for catalysis, *ACS Catal.*, 2015, **5**, 6370–6385, DOI: 10.1021/acscatal.5b01667.

4 O. V. Nkwachukwu and O. A. Arotiba, Perovskite oxide–based materials for photocatalytic and photoelectrocatalytic treatment of water, *Front. Chem.*, 2021, **9**, 634630, DOI: 10.3389/fchem.2021.634630.

5 T.-W. Chen, R. Ramachandran, S.-M. Chen, G. Anushya, S. D. Rani, V. Mariyappan, P. Elumalai and N. Vasimalai, High-performance-based perovskite-supported nanocomposite for the development of green energy device applications: an overview, *Nanomaterials*, 2021, **11**, 1006, DOI: 10.3390/nano11041006.

6 M. Christy, H. Rajan, H. Lee, I. Rabani, S. M. Koo and S. C. Yi, Surface engineering of perovskites for rechargeable zinc−air battery application, *ACS Appl. Energy Mater.*, 2021, **4**(2), 1876–1886, DOI: 10.1021/acsaem.0c02983.

7 J. Y. Kim, J.-W. Lee, H. S. Jung, H. Shin and N.-G. Park, High-efficiency perovskite solar cells, *Chem. Rev.*, 2020, **120**, 7867–7918, DOI: 10.1021/acs.chemrev.0c00107.

8 Y. Wang, Z. Lv, L. Zhou, X. Chen, J. Chen, Y. Zhou, V. A. L. Roy and S.-T. Han, Emerging perovskite materials for high density data storage and artificial synapses, *J. Mater. Chem. C*, 2018, **6**, 1600–1617, DOI: 10.1039/C7TC05326F.

9 S. M. Yakout, Spintronics: future technology for new data storage and communication devices, *J. Supercond. Nov. Magn.*, 2020, **33**, 2557–2580, DOI: 10.1007/s10948-020-05545-8.

10 G. Chen, A. Feldhoff, A. Weidenkaff, C. Li, S. Liu, X. Zhu, J. Sunarso, K. Huang, X.-Y. Wu, A. F. Ghoniem, W. Yang, J. Xue, H. Wang, Z. Shao, J. H. Duffy, K. S. Brinkman, X. Tan, Y. Zhang, H. Jiang, R. Costa, K. A. Friedrich and R. Kriegel, Roadmap for sustainable mixed ionic-electronic conducting membranes, *Adv. Funct. Mater.*, 2021, **31**, 2105702, DOI: 10.1002/adfm.202105702.

11 M. C. Knapp and P. M. Woodward, A-site cation ordering in AA'BB'O_6 perovskites, *J. Solid State Chem.*, 2006, **179**, 1076–1085, DOI: 10.1016/j.jssc.2006.01.005.

12 G. King and S. G. Martin, Expanding the doubly cation Ordered AA′BB′O_6 perovskite family: structural complexity in $NaLaInNbO_6$ and $NaLaInTaO_6$, *Inorg. Chem.*, 2019, **58**, 14058–14067, DOI: 10.1021/acs.inorgchem.9b02050.

13 Q. Liu, J. Guo, M. Fan, Q. Zhang, S. Liu, K.-L. Wong, Z. Liu and B. Wei, Fast synthesis of Dy^{3+} and Tm^{3+} co-doped double perovskite $NaLaMgWO_6$: a thermally stable single-phase white-emitting phosphor for WLEDs, *J. Mater. Chem. C*, 2020, **8**, 2117–2122, DOI: 10.1039/C9TC05592D.

14 K. Ji, J. R. Bedward, Q. Li, P. Manuel, C. Ritter and J. P. Attfield, $CaFeFeNbO_6$ – an iron-based double Perovskite, *Chem. Commun.*, 2023, **59**, 6371–6374, DOI: 10.1039/D3CC01115A.

15 T. Ahmed, A. Chen, D. A. Yarotski, S. A. Trugman, Q. Jia and J.-X. Zhu, Magnetic, electronic, and optical properties of double perovskite Bi_2FeMnO_6, *APL Mater.*, 2017, **5**, 035601, DOI: 10.1063/1.4964676.

16 M. Qu, X. Ding, Z. Shen, M. Cui, F. E. Oropeza, G. Gorni, V. A. de la Pena O'Shea, W. Li, D.-C. Qi and K. H. L. Zhang, Tailoring the electronic structures of the La_2NiMnO_6 double perovskite as efficient bifunctional oxygen electrocatalysis, *Chem. Mater.*, 2021, **33**, 2062–2071, DOI: 10.1021/acs.chemmater.0c04527.

17 B. R. Meena, M. Alam, S. Chatterjee and A. K. Ghosh, Structural, dielectric, and electrical transport properties of La_2FeMnO_6 double perovskite for multifunctional applications, *Ceram. Int.*, 2025, **51**, 7305–7320, DOI: 10.1016/j.ceramint.2024.12.166.

18 S. Y. Vilar, A. C. Couceiro, B. R. Murias, A. Fondado, J. Mira, J. Rivas and M. A. S. Rodrguez, Study of the dielectric properties of the perovskite $LaMn_{0.5}Co_{0.5}O_{3-\delta}$, *Z. Anorg. Allg. Chem.*, 2005, **631**, 2265–2272, DOI: 10.1002/zaac.200570055.

19 D. K. Pradhan, S. Kumari, V. S. Puli, P. T. Das, D. K. Pradhan, A. Kumar and R. S. Katiyar, Correlation of dielectric, electrical and magnetic properties near the magnetic phase transition temperature of cobalt zinc ferrite, *Phys. Chem. Chem. Phys.*, 2017, **19**, 210–218, DOI: 10.1039/C6CP06133H.

20 K. M. Srinivasamurthy, A. E. Denglawey, K. Manjunatha, J. Angadi V., M. C. Oliveira, E. Longo, S. R. Lazaro and R. A. P. Ribeiro, Observation of dielectric dispersion and relaxation behavior in Ni^{2+}-substituted cobalt ferrite nanoparticles, *J. Mater. Chem. C*, 2022, **10**, 3418–3428, DOI: 10.1039/D1TC05980G.

21 J. Boonlakhorn, S. Promsai, S. Khongpakdee, M. Mani, P. Khongrattana, P. Suksangrat, P. Thongbai and P. Srepusharawoot, $Li_{1/2}Y_{1/2}Cu_3Ti_4O_{12}$ Ceramic: structural, dielectric, and electrical investigations, *ACS Appl. Electron. Mater.*, 2023, **5**, 3324–3332, DOI: 10.1021/acsaelm.3c00367.

22 S. Sahoo, L. Sahoo, N. C. Nayak, B. N. Parida and R. K. Parida, Investigation of the structural, dielectric, magnetic properties and NTC-thermistor response of $CaBiFeMnO_6$ double perovskites, *Mater. Adv.*, 2024, **5**, 5442–5457, DOI: 10.1039/D4MA00175C.

23 N. A. F. M. Saadon, N. I. Taib, C. W. Loy and Z. Mohamed, Role of Ca^{2+} doping on the enhancement of dielectric properties of $Sr_{2-x}Ca_xNiWO_6$ for energy storage device application, *Sci. Rep.*, 2023, **13**, 1246, DOI: 10.1038/s41598-023-28296-7.

24 G. Takalkar, R. R. Bhosale, F. AlMomani, A. Kumar, A. Banu, A. Ashok, S. Rashid, M. Khraisheh, A. Shakoor and A. Al Ashraf, Thermochemical splitting of CO_2 using solution combustion synthesized $LaMO_3$ (where, M = Co, Fe, Mn, Ni, Al, Cr, Sr), *Appl. Surf. Sci.*, 2020, **509**, 144908, DOI: 10.1016/j.apsusc.2019.144908.

25 H. Z. Azad, A. Khodadadi, P. E. Ahranjani and Y. Mortazavi, Effects of Pd on enhancement of oxidation activity of $LaBO_3$ (B = Mn, Fe, Co and Ni) perovskite catalysts for pollution abatement from natural gas fueled vehicles, *Appl. Catal., B*, 2011, **102**, 62–70, DOI: 10.1016/j.apcatb.2010.11.025.

26 A. Ashok, A. Kumar, R. R. Bhosale, F. Almomani, S. S. Malik, S. Suslov and F. Tarlochan, Combustion synthesis of bifunctional $LaMO_3$ (M = Cr, Mn, Fe, Co, Ni) perovskites for oxygen reduction and oxygen evolution reaction in alkaline media, *J. Electroanal. Chem.*, 2018, **809**, 22–30, DOI: 10.1016/j.jelechem.2017.12.043.

27 P. Głuchowski, K. Oganisian, R. Tomala, A. Łukowiak, D. Karpinsky, D. Alikin, A. Kholkin and W. Strek, Optical, dielectric and magnetic properties of $La_{1-x}Nd_xFeO_3$ powders and ceramics, *Ceramics*, 2019, **2**(1), 1–12, DOI: 10.3390/ceramics2010001.

28 Z. Anajafi, M. Naseri and G. Neri, Optical, magnetic and gas sensing properties of $LaFeO_3$ nanoparticles synthesized by different chemical methods, *J. Electron. Mater.*, 2019, **48**, 6503–6511, DOI: 10.1007/s11664-019-07436-8.

29 W. Xia, Z. Pei, K. Leng and X. Zhu, Research progress in rare earth-doped perovskite manganite oxide nanostructures, *Nanoscale Res. Lett.*, 2020, **15**, 9, DOI: 10.1186/s11671-019-3243-0.

30 D. Yang, T. Yang, P. Mukherjee, S. E. Dutton, D. Huo and M. A. Carpenter, Strain coupling and acoustic attenuation associated with glassy magnetic phase transitions in the disordered double perovskite La_2FeMnO_6, *Phys. Rev. B*, 2019, **99**, 094314, DOI: 10.1103/PhysRevB.99.094314.

31 M. Nasir, M. Khan, S. A. Agbo, S. Bhatt, S. Kumar and S. Sen, Evidence of cluster-glass and Griffiths-like phases in partially ordered La_2FeMnO_6 double perovskite, *J. Phys. D: Appl. Phys.*, 2020, **53**, 375003, DOI: 10.1088/1361-6463/ab9263.

32 J. B. de, A. Filho, J. H. de Araújo, M. A. Morales, C. L. Firme and J. B. de Oliveira, Exchange bias and spin glass in La_2FeMnO_6 nanoparticles, *J. Magn. Magn. Mater.*, 2019, **471**, 177–184, DOI: 10.1016/j.jmmm.2018.09.093.

33 R. V. Lakshmi, P. Bera, M. Hiremath, V. Dubey, A. K. Kundu and H. C. Barshilia, Structural, magnetic, and dielectric properties of solution combustion synthesized $LaFeO_3$, $LaFe_{0.9}Mn_{0.1}O_3$, and $LaMnO_3$ perovskites, *Phys. Chem. Chem. Phys.*, 2022, **24**, 5462–5478, DOI: 10.1039/D1CP05501A.

34 B. R. Meena, S. Chatterjee and A. K. Ghosh, Insight into charge conduction and relaxation in $La_{2-x}Ca_xFeMnO_6$ solid solution double perovskites, *J. Alloys Compd.*, 2025, **1037**, 182341, DOI: 10.1016/j.jallcom.2025.182341.

35 D. Chen, Z. Ye, Y. Yang, T. Liu, J. Li, X. Liu, Y. Zuo, J. Zheng, Z. Liu and B. Cheng, Impact of strontium doping on quasi-two-dimensional perovskite layers for sky-blue light-emitting diodes, *ACS Appl. Opt. Mater.*, 2023, **1**(8), 1405–1413, DOI: 10.1021/acsaom.3c00182.

36 Z. Wei, X. Xiong, X. Chen, J. Pan, D. Cai, X. Huang, G. Han, Y. Liu, Z. Jiang and T. Fujita, The effect of Sr doping at the A-sites on the performance of $La_{0.5}Gd_{0.5}Ba_{1-x}Sr_xCo_2O_{5+\delta}$ materials for intermediate-temperature solid oxide fuel cells, *J. Alloys Compd.*, 2024, **996**, 174860, DOI: 10.1016/j.jallcom.2024.174860.

37 M. Lamhani, Z. Chchiyai, A. Elomrani, B. Manoun and A. Hasnaoui, The effect of Sr substitution on the structural and physical properties of manganite perovskites $Ca_{1-x}Sr_xMnO_{3-\delta}$ ($0 \leq x \leq 1$), *Phys. Chem. Chem. Phys.*, 2022, **24**, 19414–19431, DOI: 10.1039/D2CP01096H.

38 K. Sultan, S. Abass, F. S. Ahanger, S. F. Najar, R. Manzoor, A. A. Shah, W. Akram, S. Gulzar, I. Ahmad and F. Shafi, Temperature dependent dielectric studies of pure and Sr doped Pr_2NiMnO_6, *Phys. B*, 2024, **682**, 415877, DOI: 10.1016/j.physb.2024.415877.

39 S. Abass, A. Bagri and K. Sultan, Modifications induced in structural, electronic and dielectric properties of Nd_2NiMnO_6 double perovskite by Sr doping, *J. Alloys Compd.*, 2023, **930**, 167463, DOI: 10.1016/j.jallcom.2022.167463.

40 T. Katheriya, G. Nirala and S. Upadhyay, Establishing the correlation of negative permittivity and AC conductivity of $La_{2-x}Sr_xNiO_4$ (x = 0, 0.1, 0.3, 1.0) for microwave shielding applications, *J. Mater. Chem. C*, 2024, **12**, 8473–8484, DOI: 10.1039/D4TC00064A.

41 J. K. Murthy, K. D. Chandrasekhar, H. C. Wu, H. D. Yang, J. Y. Lin and A. Venimadhav, Antisite disorder driven spontaneous exchange bias effect in $La_{2-x}Sr_xCoMnO_6$ ($0 \leq x \leq 1$), *J. Phys.: Condens. Matter.*, 2016, **28**, 086003, DOI: 10.1088/0953-8984/28/8/086003.

42 D. Mazumdar and I. Das, Structural, magnetic, and magnetocaloric properties of the multiferroic host double perovskite compound Pr_2FeCrO_6, *Phys. Chem. Chem. Phys.*, 2021, **23**, 5596–5606, DOI: 10.1039/D0CP06447E.

43 G. K. Williamson and W. H. Hall, X-ray line broadening from filed aluminium and wolfram L'elargissement des raies de rayons x obtenues des limailles d'aluminium et de tungsten Die verbreiterung der roentgeninterferenzlinien von aluminium-und wolframspaenen, *Acta Metall.*, 1953, **1**, 22–31, DOI: 10.1016/0001-6160(53)90006-6.

44 K. Zakharchuk, A. Kovalevsky and A. Yaremchenko, Characterization of Ruddlesden-Popper $La_{2-x}Ba_xNiO_{4\pm\delta}$ nickelates as potential electrocatalysts for solid oxide cells, *Materials*, 2023, **16**(4), 1755, DOI: 10.3390/ma16041755.

45 M. N. Iliev, M. V. Abrashev, A. P. Litvinchuk, V. G. Hadjiev, H. Guo and A. Gupta, Raman spectroscopy of ordered double perovskite La_2CoMnO_6 thin films, *Phys. Rev. B: Condens. Matter Mater. Phys.*, 2007, **75**, 104118, DOI: 10.1103/PhysRevB.75.104118.

46 O. Wiranwetchayan, S. Promnopas, S. Phadungdhitidhada, A. Phuruangrat, T. Thongtem, P. Singjai and S. Thongtem, Characterization of perovskite $LaFeO_3$ synthesized by microwave plasma method for photocatalytic applications, *Ceram. Int.*, 2019, **45**, 4802–4809, DOI: 10.1016/j.ceramint.2018.11.175.

47 D. Triyono, Y. Yunida and R. A. Rafsanjani, Effect of Heat Treatment on structural, magnetic and electrical properties of La_2FeMnO_6, *Materials*, 2021, **14**(24), 7501, DOI: 10.3390/ma14247501.

48 A. Pal, P. Singh, V. K. Gangwar, A. G. Joshi, P. Khuntia, G. D. Dwivedi, P. K. Gupta, M. Alam, K. Anand, K. Sethupathi,

A. K. Ghosh and S. Chatterjee, Probing the Griffiths like phase, unconventional dual glassy states, giant exchange bias effects and its correlation with its electronic structure in $Pr_{2-x}Sr_xCoMnO_6$, *J. Phys.: Condens. Matter*, 2020, **32**, 215801, DOI: 10.1088/1361-648X/ab5326.

49 J.-Y. Baek, L. T. Duy, S. Y. Lee and H. Seo, Aluminum doping for optimization of ultrathin and high-*k* dielectric layer based on $SrTiO_3$, *J. Mater. Sci. Technol.*, 2020, **42**, 28–37, DOI: 10.1016/j.jmst.2019.12.006.

50 C. Maccato, G. Carraro, D. Peddis, G. Varvaro and D. Barreca, Magnetic properties of ε iron(III) oxide nanorod arrays functionalized with gold and copper(II) oxide, *Appl. Surf. Sci.*, 2018, **427**, 890–896, DOI: 10.1016/j.apsusc.2017.09.015.

51 E. Cao, Y. Yang, T. Cui, Y. Zhang, W. Hao, L. Sun, H. Peng and X. Deng, Effect of synthesis route on electrical and ethanol sensing characteristics for $LaFeO_{3-\delta}$ nanoparticles by citric sol–gel method, *Appl. Surf. Sci.*, 2017, **393**, 134–143, DOI: 10.1016/j.apsusc.2016.10.013.

52 P. W. Menezes, A. Indra, V. Gutkin and M. Driess, Boosting electrochemical water oxidation through replacement of O_h Co sites in cobalt oxide spinel with manganese, *Chem. Commun.*, 2017, **53**, 8018–8021, DOI: 10.1039/C7CC03749J.

53 Y. Bai, Y. Xia, H. Li, L. Han, Z. Wang, X. Wu, S. Lv, X. Liu and J. Meng, A-site-doping enhanced B-Site ordering and correlated magnetic property in $La_{2-x}Bi_xCoMnO_6$, *J. Phys. Chem. C*, 2012, **116**, 16841–16847, DOI: 10.1021/jp302735x.

54 S. Sharma, V. Singh, R. K. Kotnala and R. K. Dwivedi, Comparative studies of pure $BiFeO_3$ prepared by sol–gel versus conventional solid-state-reaction method, *J. Mater. Sci.: Mater. Electron.*, 2014, **25**, 1915–1921, DOI: 10.1007/s10854-014-1820-7.

55 G. S. Rao, C. N. R. Rao and J. R. Ferraro, Infrared and Electronic Spectra of Rare Earth Perovskites: *Ortho*-Chromites, -Manganites and -Ferrites, *Appl. Spectrosc.*, 1970, **24**(4), 436–445, DOI: 10.1366/000370270774371426.

56 S. K. Deshpande, S. N. Achary, R. Mani, J. Gopalakrishnan and A. K. Tyagi, Low-temperature polaronic relaxations with variable range hopping conductivity in $FeTiMO_6$ (M = Ta, Nb, Sb), *Phys. Rev. B: Condens. Matter Mater. Phys.*, 2011, **84**, 064301, DOI: 10.1103/PhysRevB.84.064301.

57 M. Islam, S. K. Adhikari, S. Adhikari, S. Chatterjee, S. Goswami, D. De, K. A. Irshad, B. Joseph, W. Caliebe and A. Karmakar, Charge conduction and relaxation in $Ca_{1-x}Dy_xBaFe_4O_7$, *Phys. Rev. B: Condens. Matter Mater. Phys.*, 2025, **111**, 054110, DOI: 10.1103/PhysRevB.111.054110.

58 S. Khadhraoui, A. Triki, S. Hcini, S. Zemni and M. Oumezzine, Variable-range-hopping conduction and dielectric relaxation in $Pr_{0.6}Sr_{0.4}Mn_{0.6}Ti_{0.4}O_{3\pm\delta}$ perovskite, *J. Magn. Magn. Mater.*, 2014, **371**, 69–76, DOI: 10.1016/j.jmmm.2014.07.044.

59 W. Hizi, H. Rahmouni, K. Khirouni and E. Dhahri, Consistency between theoretical conduction models and experimental conductivity measurements of strontium-doped lanthanum manganite, *J. Alloys Compd.*, 2023, **957**, 170418, DOI: 10.1016/j.jallcom.2023.170418.

60 W. Hizi, M. Wali, H. Rahmouni, K. Khirouni and E. Dhahri, Examination of charge-carriers hopping and identification of relaxation phenomenon and blocking effect in perovskite system, *Eur. Phys. J. Plus*, 2024, **139**, 156, DOI: 10.1140/epjp/s13360-024-04968-9.

61 D. Liu, S. J. Clark and J. Robertson, Oxygen vacancy levels and electron transport in Al_2O_3, *Appl. Phys. Lett.*, 2010, **96**, 032905, DOI: 10.1063/1.3293440.

62 A. P. Barranco, J. D. S. Guerra, R. L. Noda and E. B. Araújo, Ionized oxygen vacancy-related electrical conductivity in $(Pb_{1-x}La_x)(Zr_{0.90}Ti_{0.10})_{1-x}/4O_3$ ceramics, *J. Phys. D: Appl. Phys.*, 2008, **41**, 215503, DOI: 10.1088/0022-3727/41/21/215503.

63 H. Zheng, W. Weng, G. Han and P. Du, Colossal permittivity and variable-range-hopping conduction of polarons in $Ni_{0.5}Zn_{0.5}Fe_2O_4$ Ceramic, *J. Phys. Chem. C*, 2013, **117**, 12966–12972, DOI: 10.1021/jp402320b.

64 K. S. Cole and R. H. Cole, Dispersion and absorption in dielectrics I. alternating current characteristics, *J. Chem. Phys.*, 1941, **9**, 341–351, DOI: 10.1063/1.1750906.

65 S. Hunpratub, P. Thongbai, T. Yamwong, R. Yimnirun and S. Maensiri, Dielectric relaxations and dielectric response in multiferroic $BiFeO_3$ ceramics, *Appl. Phys. Lett.*, 2009, **94**, 062904, DOI: 10.1063/1.3078825.

66 X.-Z. Chen, R.-L. Yang, J.-P. Zhou, X.-M. Chen, Q. Jiang and P. Liu, Dielectric and magnetic properties of multiferroic $BiFeO_3$ ceramics sintered with the powders prepared by hydrothermal method, *Solid State Sci.*, 2013, **19**, 117–121, DOI: 10.1016/j.solidstatesciences.2013.02.012.

67 Z. Wang, K. Sun, P. Xie, Q. Hou, Y. Liu, Q. Gu and R. Fan, Design and analysis of negative permittivity behaviors in barium titanate/nickel metacomposites, *Acta Mater.*, 2020, **185**, 412–419, DOI: 10.1016/j.actamat.2019.12.034.

68 P. Yang, K. Sun, Y. Wu, H. Wu, X. Yang, X. Wu, H. Du and R. Fan, Negative permittivity behaviors derived from dielectric resonance and plasma oscillation in percolative bismuth ferrite/silver composites, *J. Phys. Chem. C*, 2022, **126**, 12889–12896, DOI: 10.1021/acs.jpcc.2c03543.

69 M.-R. Zhang and Y. Su, The negative dielectric permittivity of polycrystalline barium titanate nanofilms under high-strength kHz-AC fields, *Int. J. Solids Struct.*, 2022, **111939**, 254–255, DOI: 10.1016/j.ijsolstr.2022.111939.

70 H. Meena, S. Mishra, D. Gupta, B. R. Meena and H. Kumar, Effect of Bi modification on structural and dielectric properties of selenium-rich Se–In chalcogenide glasses, *Ceram. Int.*, 2025, **51**, 12634–12644, DOI: 10.1016/j.ceramint.2025.01.103.

71 A. Manan, A. Ullah, M. A. Khan, A. S. Ahmad, Y. Iqbal, I. Qazi, M. Rehman, A. Ullah and H. Liu, Preparation, characterization, and improvement in the energy storage properties of $Bi(Li_{0.5}Ta_{0.5})O_3$ modified $Na_{0.5}K_{0.5}NbO_3$ ceramic system, *Mater. Res. Bull.*, 2022, **145**, 111521, DOI: 10.1016/j.materresbull.2021.111521.

72 G.-F. Zhang, H. Liu, Z. Yao, M. Cao and H. Hao, Effects of Ca doping on the energy storage properties of (Sr, Ca)TiO_3 paraelectric ceramics, *J. Mater. Sci.: Mater. Electron.*, 2015, **26**, 2726–2732, DOI: 10.1007/s10854-015-2749-1.

73 H. Choi, S. Pattipaka, Y. H. Son, Y. M. Bae, J. H. Park, C. K. Jeong, H. E. Lee, S.-D. Kim, J. Ryu and G.-T. Hwang, Improved energy storage density and efficiency of Nd and Mn Co-doped $Ba_{0.7}Sr_{0.3}TiO_3$ ceramic capacitors via defect dipole engineering, *Materials*, 2023, **16**, 6753, DOI: 10.3390/ma16206753.

74 M. Sahu, S. Hajra, K. Mohanta, V. Purohit and R. N. P. Choudhary, Dielectric and impedance spectroscopy of aluminium oxide substituted fused silica samples, *SN Appl. Sci.*, 2019, **1**, 1254, DOI: 10.1007/s42452-019-1290-x.

75 B. Prajapati, S. Kumar, M. Kumar, S. Chatterjee and A. K. Ghosh, Investigation of the physical properties of Fe: TiO_2-diluted magnetic semiconductor nanoparticles, *J. Mater. Chem. C*, 2017, **5**, 4257, DOI: 10.1039/C7TC00233E.

76 T. Plutenko, O. V'yunov, O. Fedorchuk, B. Khomenko and A. Belous, Sol–gel synthesis, structure, and dielectric properties of $La_{0.67}Li_xTi_{1-x}Al_xO_3$ solid solutions, *Heliyon*, 2023, **9**, e15392, DOI: 10.1016/j.heliyon.2023.e15392.

77 MakeItFrom.com. "MakeItFrom.com: Material Properties Database." MakeltFrom.com, 30 May 2020, https://www.makeitfrom.com/material-properties/Steatite. Accessed 17 October 2025.

78 MakeItFrom.com. "MakeItFrom.com: Material Properties Database." MakeltFrom.com, 30 May 2020, https://www.makeitfrom.com/material-properties/Alumina-Aluminum-Oxide-Al2O3, Accessed 17 October 2025.

79 MakeItFrom.com. "MakeItFrom.com: Material Properties Database." MakeltFrom.com, 30 May 2020, https://www.makeitfrom.com/material-properties/Zirconia-Zirconium-Dioxide-ZrO2, Accessed 17 October 2025.

80 MakeItFrom.com. "MakeItFrom.com: Material Properties Database." MakeltFrom.com, 30 May 2020, https://www.makeitfrom.com/material-properties/Zircon-Zirconium-Silicate-ZrSiO4, Accessed 17 October 2025.

81 MakeItFrom.com. "MakeItFrom.com: Material Properties Database." MakeltFrom.com, 30 May 2020, https://www.makeitfrom.com/material-properties/Engineering-Porcelain, Accessed 17 October 2025.

82 R. F. Blunt and W. F. Love, The dielectric properties of barium titanate at low temperatures, *Phys. Rev.*, 1949, **76**, 1202, DOI: 10.1103/PhysRev.76.1202.

83 L. Boudad, M. Taibi, A. Belayachi and M. Abd-lefdil, Structural, morphological, dielectric and optical properties of double perovskites $RBaFeTiO_6$ (R = La, Eu), *RSC Adv.*, 2021, **11**, 40205, DOI: 10.1039/D1RA06793A.

84 Q. Tang and X. Zhu, Structural characterization and physical properties of double perovskite $La_2FeReO_{6+\delta}$ powders, *Nanomaterials*, 2022, **12**, 244, DOI: 10.3390/nano12020244.

85 S. Das, R. C. Sahoo, S. Mishra, D. Bhattacharya and T. K. Nath, Effects of Ni doping at Co site on dielectric, impedance spectroscopy and AC conductivity in La_2CoMnO_6 double perovskites, *Appl. Phys. A*, 2022, **128**, 354, DOI: 10.1007/s00339-022-05489-x.

86 R. Datta, S. K. Pradhan, S. Majumdar and S. K. De, Dielectric and impedance spectroscopy of Nd_2CoIrO_6 double perovskite, *J. Phys.: Condens. Matter*, 2020, **32**, 495702, DOI: 10.1088/1361-648X/abaf92.

87 K. S. Hemalatha, G. Sriprakash, M. V. N. A. Prasad, R. Damle and K. Rukmani, Temperature dependent dielectric and conductivity studies of polyvinyl alcohol-ZnO nanocomposite films by impedance spectroscopy, *J. Appl. Phys.*, 2015, **118**, 154103, DOI: 10.1063/1.4933286.

88 J. A. Bittencourt, *Fundamentals of plasma physics*, Springer-Verlag, New York, 3rd edn, 2004.

89 S. Vangchangyia, E. Swatsitang, P. Thongbai, S. Pinitsoontorn, T. Yamwong, S. Maensiri, V. Amornkitbamrung and P. Chindaprasirt, Very low loss tangent and high dielectric permittivity in pure-$CaCu_3Ti_4O_{12}$ ceramics prepared by a modified sol-gel process, *J. Am. Ceram. Soc.*, 2012, **95**, 1497–1500, DOI: 10.1111/j.1551-2916.2012.05147.x.

90 M. Abazari and A. Safari, Leakage current behavior in lead-free ferroelectric (K, Na)NbO_3–$LiTaO_3$–$LiSbO_3$ thin films, *Appl. Phys. Lett.*, 2010, **97**, 262902, DOI: 10.1063/1.3531575.

91 G. W. Pabst, L. W. Martin, Y.-H. Chu and R. Ramesh, Leakage mechanisms in $BiFeO_3$ thin films, *Appl. Phys. Lett.*, 2007, **90**, 072902, DOI: 10.1063/1.2535663.

92 G.-Y. Zhang, J.-Q. Dai and Y.-S. Lu, Phase structure and electrical properties of $(1-x)Bi_{1+y}FeO_{3-x}BaTiO_3$ lead-free ceramics with different Bi contents, *J. Mater. Sci.: Mater. Electron.*, 2021, **32**, 10289–10298, DOI: 10.1007/s10854-021-05684-1.

93 H. Yang, F. Yan, Y. Lin, T. Wang and F. Wang, High energy storage density over a broad temperature range in sodium bismuth titanate-based lead-free ceramics, *Sci. Rep.*, 2017, **7**, 8726, DOI: 10.1038/s41598-017-06966-7.

94 S. Malik and A. Dutta, Structural, electrical, leakage current, and magnetic characteristics of double perovskite Nd_2NiTiO_6, *J. Am. Ceram. Soc.*, 2025, **108**, e20150, DOI: 10.1111/jace.20150.

95 A. Z. Simões, L. S. Cavalcante, F. Mourac, E. Longo and J. A. Varela, Structure, ferroelectric/magnetoelectric properties and leakage current density of $(Bi_{0.85}Nd_{0.15})FeO_3$ thin films, *J. Alloys Compd.*, 2011, **509**, 5326–5335, DOI: 10.1016/j.jallcom.2011.02.030.